Arab American University-Jenin

Faculty of Graduate Studies

Physical Design and Characterization of Ge/InSe/Ga_2S_3 Hybrid Devices

By

Olfat Abdulfatah Omareya

Supervisor

Prof. Dr. Atef Fayez Qasrawi

This thesis was submitted in partial fulfillment of the requirements for

The Master's degree in

Physics

July/2017

Physical Design and Characterization of Ge/InSe/Ga_2S_3 Hybrid Devices

By

Olfat Abdulfatah Omareya

This thesis was defended successfully on July 8th 2017 and approved by:

Committee members Signature

1. Prof. Dr. Atef Fayez Qasrawi (Supervisor) …….

2. Assoc. Prof. Dr. Adli A. Saleh (Internal examiner) …….

3. Assoc. Prof. Dr. Khaled Ilaiwi (External examiner) …….
(An Najah National University)

Declaration

The work in this thesis, unless otherwise referenced, is the researcher's own work and has not been submitted elsewhere for any other degree or qualification.

أقر بأن ما اشتملت عليه هذه الرسالة إنما هو نتاج جهدي الخاص، باستثناء ما تمت الإشارة إليه حيثما ورد، وأن هذه الرسالة ككل من أو أي جزء منها لم يقدم من قبل للحصول على أية درجة أو بحث علمي لدى أي مؤسسة تعليمية أو بحثية أخرى.

Student's Name:

Signature:

Date:

To My Parents

Acknowledgments

First and foremost, I praise God, the almighty for giving me this chance and granting me the capability for its success. This current form of my thesis is due to the guidance and helping of many people. So I would like to offer my thanks to all of them.

Starting with endless thanks for my supervisor Prof. Dr. Atef Fayez Qasrawi, who didn't hold back any efforts in warm encouragement, continuous support, patience and kind communication that made a great effect regarding to feel interesting about what I'm working on. It is not often that one can find a person to be advisor and colleague that always creates the time for listening to the little problems and roadblocks that are unavoidably faced in the research performing. His critical comments and correction were important to the completion of this work and has taught me unnumbered lessons on the academic research workings. He grants me an ideal balance of freedom to my own ideas in order to guide me to the right direction allowing independent conceptualization of my research problem. I cannot thank him enough for his knowledge and guidance throughout the years.

My many thanks to Dr. Hazem Khanfer; the member of Department of Telecommunication Engineering and member of Research LAB at Arab American University, for his technical advices. The depth of his software knowledge has helped me greatly in dealing with instruments.

My genuine thanks to all department members: Prof. Dr. Zaki Saleh, Dr. Adli Saleh, Dr. Muayad Abu Saa, Dr. Ahmad Omar, Prof. Mohammad Abu Samra, Dr. Soliman Rabaa, and Mr. Anan Hussien.

I wish to express my sincere thanks to internal examiner Dr. Adli Saleh and external examiner Dr. Khaled Ilaiwi for their support, valuable suggestions and critical comments.

The friendship of Eman Nazzal is much appreciated and has led to good-spirited discussions relating to this research. Many thanks for her suggestions and help during my thesis writing.

I cannot forget all friends who went together through hard times, cheered me up, and celebrated each achievement.

I have no words in my dictionary to express my thanks to my brothers and sister. Lamees, Ibrahim, Ihsan, Arkan and Osaid, for their constant support. They were one of the first friendly faces to greet me when I began this master's thesis.

Last, but not least. I want to express my deepest gratitude to my parents for their instillation of many admirable qualities in me and for the many years of their dedication and support during my studies.

Physical Design and Characterization of Ge/InSe/Ga_2S_3 Hybrid Devices

By

Olfat Abdulfatah Omareya

Supervisor

Prof. Dr. Atef Fayez Qasrawi

Abstract

In this thesis, the design and characterization of metal-heterojunction-metal structure were studied as a $n^+ - p$ junction device. In the growth process, the n −type InSe (200 nm) was deposited onto a p −Ge film of 200 nm thickness. The Ge/InSe interface was used as substrate to evaporate the n −Ga_2S_3 films of 200 nm thickness. The interface was structurally, optically and electrically characterized by means of scanning electron microscopy, energy dispersive X-ray analysis (EDX), X-ray diffraction, UV-visible spectrophotometry, impedance spectroscopy and current-voltage characteristics. The X-ray diffraction patterns which were collected from the surface of the Ge/Ga_2S_3 and InSe/Ga_2S_3 indicated a polycrystalline nature of the heterojunctions with the domination of diamond Ge structure in the Ge/Ga_2S_3 interface and the domination of the monoclinic α-Ga_2S_3 in the Ge/Ga_2S_3 interface. The EDX analysis proved the physical nature of formation of the layers with the correct stoichiometric composition. In addition, the optical transmittance and reflectance spectral analysis revealed wide band gap attenuation upon layers interfacing. The conduction and valence offsets calculations indicated values that are large enough to actualize quantum confinement of holes and electrons to illuminate direct carrier recombination and as a result enhances the light absorbance. The dielectric performance of

the hybrid device was evaluated through the Drude-Lorentz modeling which reveals electron-plasmon interactions through scattering times of femtosecond level leading to a drift mobility of 27.4 cm^2/Vs. The maximum plasmon frequency for the three layers was in the range 1.8-3.8 GHz. Moreover, the impedance spectral measurements in the range of 10-1800 MHz indicated negative capacitance effect associated with parallel and series resonance at ~180 MHz. The return loss and reflection coefficient in that range behaved as a band stop filter with spectral width of 1400 MHz. Furthermore, the sandwiching of the hybrid device between two electrodes of aluminum revealed a back-to-back Schottky device that conducts current via Richardson-Schottky mechanism in which carriers have sufficient energy to overcome the barriers. The Ge/InSe/Ga_2S_3 device seems to be promising as a thin film transistor which can perform as plasmonic device and microwave resonator as well.

List of contents

List of tables

List of figures

Chapter One
Introduction and Literature Survey

Germanium (Ge) is one of the most important materials in modern technology, especially in nanoscience researching. It is environmentally friendly semiconductor material, which can be a promising electrode for applications where rate capability, durability and high energy density are important, like energy storage devices for space applications [1]. Ge has a narrow energy band gap of 0.70 eV. Thus, Ge interface with wide energy band gap materials are reported to be promising for the microwave resonators applications. For example, Ge/boron nitride (BN) interface exhibited a microwave band stop filter properties [2]. In addition, the dispersive optical parameters indicate the applicability of the Ge thin films in terahertz sensing technology with a wide range of applications in medical and telecommunication fields [3].

On the other hand, indium selenide (InSe) which has novel characteristics reflect much attention for its photovoltaic and wave trap potential application. It is very attractive material that can be used to fabricate new types of optoelectronic devices and solid state batteries in the form of thin films [4]. Two-dimensional InSe crystal was claimed to have properties which make it a promising candidate to produce the next-generation of ultrathin and flexible optoelectronic devices [5]. γ-In_2Se_3 is used like window layer (1.8 eV band gap) and β-In_2Se_3 (1.55 eV) as absorber layer in solar cells [4].

The electronic properties of the device and the deposition interface morphology of the metal/InSe indicated that the contact interface between the metals and InSe play main role in forming low resistance interfaces. This paves InSe applications in nano-electrical devices. It provides general guidelines and rules on the optimum design of low resistance contacts for

high performance field effect transistors FETs [6]. Moreover, the SnO_2/p-InSe/Ag Schottky structure is reported to provide an excellent rectification ratio [7]. It is mentioned that Al/InSe/BN/Ag heterojunctions made the device exhibit switching properties and band stop filtering properties. These features indicated the ability to use these devices in communication systems [8].

In addition to the Ge and InSe, gallium sulfide (Ga_2S_3) is a wide band gap semiconductor (3.42 eV) which finds applications in similar technologies. The nonlinear optical analysis on Ga_2S_3 nominates it as large second-harmonic generator suited terahertz application [9-12]. Ga_2S_3 is a III-VI defect semiconductor that exhibits monoclinic, hexagonal, and cubic crystal structures. Among these, the monoclinic phase is the most stable crystal structure of Ga_2S_3 [10]. The values of dielectric parameters of Ga_2S_3 indicated that nominate the Ga_2S_3 thin films as effective candidates in thin film transistor and gas sensing technologies [13].

The Ge, InSe and Ga_2S_3 films obtained by a various number of deposition techniques, such as, sol-gel process, thermal evaporation under vacuum, sputtering, molecular beam epitaxy (MBE), and physical or chemical vapor deposition [14]. Some of techniques are excellent and common used in semiconductor technology like vacuum evaporation. Physics of thin film evaporation plays an essential role for designing systems of highly efficient micro-scale thermal management [15].

In this thesis, we discuss the problem of designing a hybrid device, which behaves as p-n^+ device. Particularly, the physical nature of design, the optical characteristics and dielectric performance, in addition to the electrical and impedance spectroscopy will be explored by means of x-ray, SEM, EDX, UV-VIS and impedance spectroscopy techniques.

The second chapter of this thesis will focus on some of the theoretical relations that are in needed for predicting the experimental results. In the following chapter (chapter 3), the experimental procedures that are used to handle the measurements, are reported and explained some of the schematic presentation of the measuring devices will be shown.

In chapter 4, the revealed results are considered in details, some of the optical data is also subjected to computational analysis to obtain the operative range of the hybrid device. As a practical application in microwave technology the main parameters presented by the impedance match and reflection coefficient as well as the return loss will be discussed. The conclusions that are derived from these results will be shown in chapter 5.

Chapter Two
Theoretical Background

2.1: The x-ray diffraction

The X-ray region usually considered to be the part of the electromagnetic spectrum lying in between 0.1-100 Å. The interatomic distances are normally of the order of a few angstrom, therefore the standard optical microscope measurements do not provide sufficient information on the crystal structure. However, X-rays with a few angstroms wavelengths can do. When a beam of monochromatic x-ray falls onto a material, constructive interference after scattering only appears when the path of the partial waves on the lattice planes *n* differ by one or more wavelengths. The maximum conditions for a beam diffracted by atomic planes (shown in figure 2.1) are given by the Bragg equation [16]:

$$n\lambda = 2d \sin\theta \qquad (2.1)$$

Where *n* is an integer represents the order of reflection maximum, λ is the wavelength of the incoming x-rays, *d* is the interplanar spacing between successive atomic planes, and is d and θ is the angle of incidence, that equals the angle of reflection.

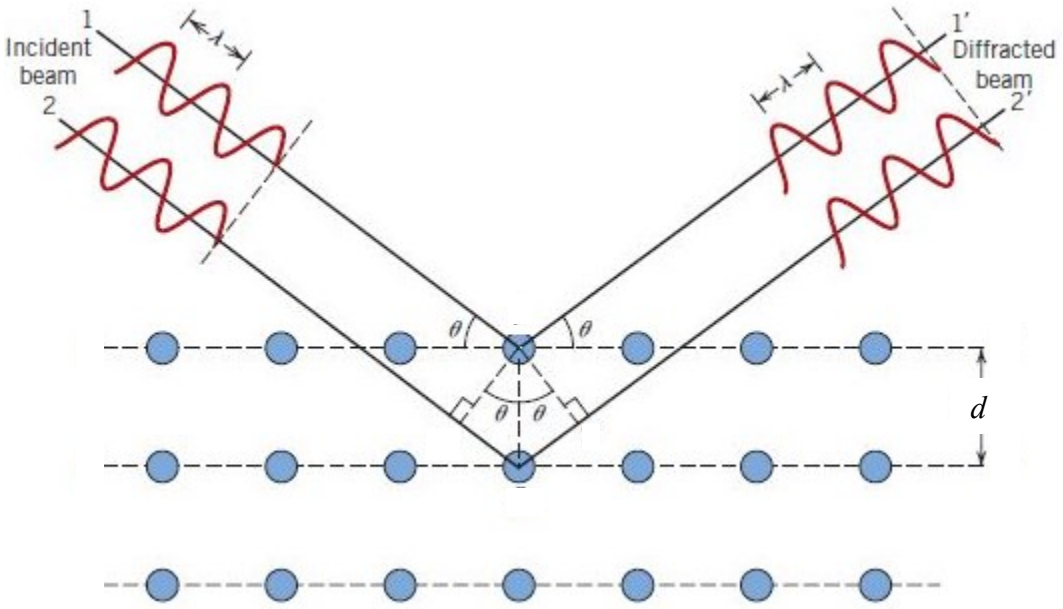

Fig. 2.1: Bragg scattering on the lattice surface.

Other structural parameters can be found using Scherrer equation, which was developed in 1918, it relates the crystallites grain size to the broadening of a diffraction peak.

$$\beta \cos\theta = \frac{K\lambda}{D} + 4\varepsilon \sin\theta \qquad (2.2)$$

Where D is the grain size of the crystallites, β is the full width at half maximum intensity of peaks in radians, K is a constant related to crystallite shape, taken as 0.94 [16]. This equation has limitation presented by the grain size value which indicate the validity of the equation below 200 nm only.

2.2: Identification of dislocation density

A dislocation is a defect or irregularity within a crystal structure. The existence of dislocations influences many of the properties of materials. The density of dislocation is the total length of dislocation lines per unit area calculated by using the following equation [17]:

$$\delta = \frac{15\varepsilon}{aD}\ (lines/cm^2) \qquad (2.3)$$

Where ε is the strain, a is the lattice constant and D is the crystallite grain size. It is found from the equation (2.2), as the strain increases, the dislocation density increases, indicating a crystallite with small strength.

2.3: Drude-Lorentz model

Drude developed his model to describe the refraction complex index and dielectric constant of metals and their variations with the incident light frequency. The model treats the valence electrons as free particles. It is mostly suited for metals that have bound electrons which are treated as damped harmonically particles undergo to external electric field. The Drude model needed to be modified and adapted by adding the Lorentz model to be used for semiconductors if the free carrier density introduced through doping is sufficiently high to cause the semiconductor behaves similarly to the metal [18, 19]. The dielectric function described by the Drude-Lorentz model can used to obtain the dispersion relation [20]:

$$\varepsilon(w) = 1 - \sum_{i}^{N} \frac{{w_{pe_i}}^2}{(w^2 + iw\gamma_i)} + \sum_{i}^{N} \frac{{w_{pe_i}}^2}{\left({w_{e_i}}^2 - w^2\right) + iw\gamma_i} \qquad (2.4)$$

Where i refer to the relative peak. $w_{pe} = \sqrt{4\pi ne^2/m^*}$ is the electron bounded plasma frequency. n and m* are the free electron density and the effective mass of free electrons, respectively. w_e being the reduced resonant frequency, and γ is the damping rate.

This model enables taking advantage of semiconductors at optical frequencies and searching for a possibility of an optical plasmon existence in that range.

2.4: Optical properties in semiconductor

When a beam of light with intensity I_o strikes a sample of thickness d, it is reflected by R part of its original intensity. It also maintains *(1-R)* of its original intensity when entering the sample. After that, a portion of the beam that enters the material propagates through the sample has an absorbed intensity multiplied by a factor ($e^{-\alpha d}$), where α is the absorption coefficient.

The absorption coefficient can be used to visualize the energy band gap of semiconductors in which the Tauc's relation is employed [21, 22]:

$$(h\nu)^{1/p} \propto \left(E - E_g\right) \tag{2.5}$$

Where $h\nu$ is the photon energy and p takes values of 3, 2, 3/2, or 1/2, corresponding to indirect forbidden, indirect allowed, direct forbidden, and direct allowed transitions, respectively. Tauc plots $(\alpha E)^{1/p}$-E give the Eg from the intercept on the E-axis in the linear region of the absorption onset with the baseline.

2.5: LRC tank

An electrical circuit (LRC) consists of an inductor (L), a resistor (R), and a capacitor (C), connected in series or in parallel.

2.5.1: The series LRC circuit

In the series LRC circuit (figure 2.2), the current of each component being the same in amplitude, but the magnitude of the source voltage (V_S) is made up of the three individual element voltages, V_L, V_R and V_C.

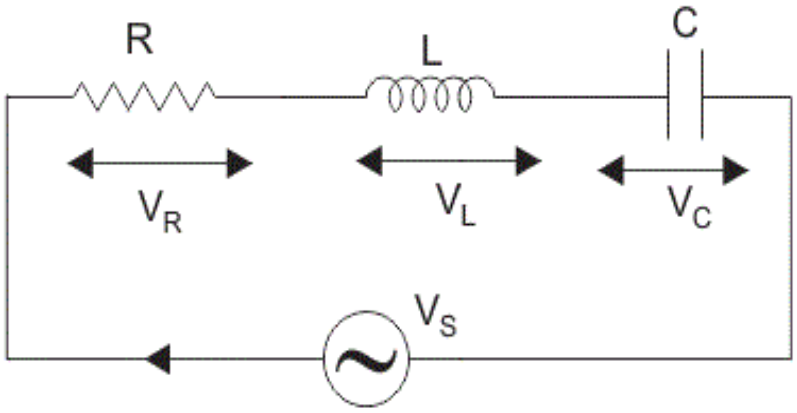

Fig. 2.2: The series LRC circuit

The source voltage is given by:

$$V_L = I\omega L, V_R = IR, V_C = {}^{I}/_{\omega C} \tag{2.6}$$

As a result, V_S is found as the Phasor Sum of the three component voltages combined together vectorially by applying Kirchoff's voltage law [23], getting:

$$V_S = IR + L\frac{dI}{dt} + \frac{Q}{C} \tag{2.7}$$

Voltage triangle for a series LRC circuit gives that:

$$V_S = \sqrt{{V_R}^2 + (V_L - V_C)^2} = I\sqrt{R^2 + (X_L - X_C)^2} = I.Z \tag{2.8}$$

The amplitude of the source voltage is proportional to the amplitude of the current with proportionality constant called the impedance of the circuit. It is the total opposition to the flow of circuit current. The overall impedance depends on the resistance and the inductive and capacitive reactances of the circuit by the relation which can be represented by an impedance triangle as shown in figure 2.3 [24].

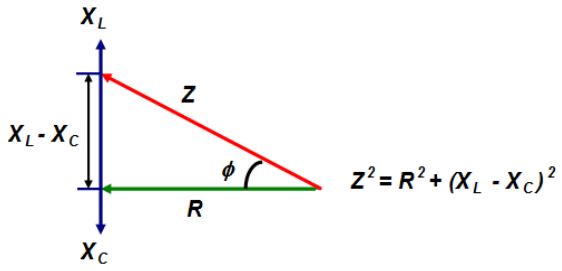

Fig. 2.3: The impedance triangle of series LRC circuit

If the inductive reactance (X_L) is greater than the capacitive reactance (X_C), then the total reactance of the circuit is inductive. However, the overall circuit reactance is capacitive if the capacitive reactance is greater than the inductive reactance.

2.5.2: The parallel LRC circuit

The source voltage is the same for all three components whereas the supply current I_S will be the vector sum of the three individual branch currents I_L, I_R and I_C. This circuit is shown in figure 2.4.

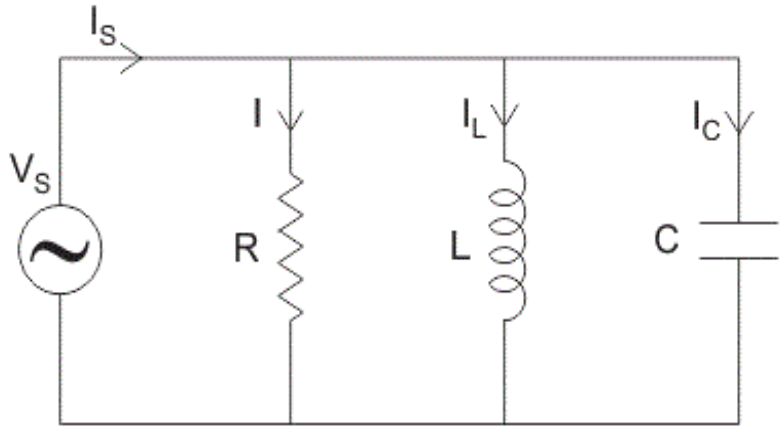

Fig. 2.4: The parallel LRC circuit

The current through each branch is found using Kirchoff's Current Law [23] again,

$$I_S = \frac{1}{RC}\frac{dV}{dt} + \frac{V}{LC} + C\frac{d^2V}{dt^2} \tag{2.9}$$

By the current triangle we get

$$I_s = \sqrt{{I_R}^2 + (I_L - I_C)^2} = \sqrt{\left(\frac{V}{R}\right)^2 + \left(\frac{V}{X_L} - \frac{V}{X_C}\right)^2} = \frac{V}{Z} \tag{2.10}$$

Where $I_R = \frac{V}{R}$, $I_L = \frac{V}{X_L}$, $I_C = \frac{V}{X_C}$

The combination of X_L, X_C and R gives the circuit impedance Z by the relation:

$$Z = \frac{1}{\sqrt{\left(\frac{1}{R}\right)^2 + \left(\frac{1}{X_L} - \frac{1}{X_C}\right)^2}} \tag{2.11}$$

It is seen that series and parallel LRC circuits contain inductive reactance and capacitive reactance within the same circuit. When the frequency varies across circuits there must be a

point where a minimum impedance take place (Z=R). The frequency at which this condition is satisfied is called resonant frequency.

2.5.3: Voltage standing wave ratio (*VSWR*)

VSWR is a way to measure transmission line imperfections. It is the ratio of the highest voltage anywhere along the transmission line to the lowest one. In a typical system, an exact match occurs between the source's impedance (Z_o) and the load's impedance (Z_L). However, mismatched impedances in real systems cause some of the power to be reflected back toward the source, leading to constructive and destructive interference, thereby peaks and valleys in the voltage occur at various times and distances along the line [25].

VSWR is related to the magnitude of the voltage reflection coefficient ($|\Gamma|=\rho$) by:

$$VSWR = \frac{1 + |\Gamma|}{1 - |\Gamma|} \tag{2.12}$$

The reflection coefficient is calculated from the impedance of the transmission (Z_o) line and the impedance of the load (Z_L) as follows in equation (2.13). The smallest reflection coefficient, the better matches. The reflection coefficient is a complex quantity, has magnitude ρ and angle Θ. It takes values from −1 for shorts and +1 for open loads, for loads $< Z_0$ it stays negative, positive for loads $> Z_0$ and zero for perfect matches [26]:

$$\Gamma = \frac{(Z_L - Z_o)}{(Z_L + Z_o)} \tag{2.13}$$

The return loss is the loss of power in the signal returned by a discontinuity in a transmission line, so the higher the absolute value of the return loss (i.e.: > |20| dB) imply the better match. The return loss (expressed in dB) makes use of ρ to be [25]:

$$Lr = -20\log(|\Gamma|) \qquad (2.14)$$

Note that in a matched load ρ=0 and return loss is ∞; in a mismatched load ρ=1 return loss is 0 dB.

2.6: Current conduction mechanisms in solids

The current transport in Schottky barriers is mainly due to majority carriers in contrast to pn junctions where minority carriers are responsible. The majority carrier current in Schottky barriers can be listed as follow:

2.6.1: Diffusion and drift currents

The diffusion current is caused by diffusion of charge carriers, it is proportional to the charge concentration gradient.

The drift current results from the motion of charge carriers by applying external electric field, it is proportional to the inversion charge concentration.

2.6.2: Thermionic emission mechanism

The thermionic emission theory is the majority carrier current and is associated with a potential barrier ϕ_0. The barrier height is much larger than kT. The current-voltage characteristics according to the thermionic emission theory are given by [27]:

$$I = AA^{**}T^2V^{\gamma}exp\left(\frac{q\phi}{kT}\right) \quad (2.15)$$

Where k and T are Boltzmann's constant and the device temperature, respectively. Here ϕ is the field-dependent activation energy that indicates a Schottky-barrier height in the presence of the electric field, A is the device area, A^{**} is Richardson constant, $\gamma = 0$.

In other words, the current transport in Richardson mechanism is limited by thermally emitted carriers from trapped centers under a strong electric field. The trap must be positively charged when empty and neutral when it traps an electron. Also, the potential height (ϕ_0) is given by equation (2.16) [28, 29].

$$\phi = \phi_0 - n\left(\frac{q\eta}{4\pi\varepsilon_o\varepsilon_r}\right)^{1/2}\frac{1}{\sqrt{w}}\sqrt{V} \quad (2.16)$$

Here q is the electronic charge. ϕ is the field-dependent activation energy that indicates a Schottky-barrier height in the presence of the electric field, Φ_0 is the no-electric-field value of barrier height which has been created at the p/n interface for the lattice mismatch, ε_r is optical dielectric constant of the material and w the effective width of the interface depletion region. When Schottky-type emission is dominant $n = \eta = 1$[30].

2.6.3: Tunneling current mechanism

For more heavily doped semiconductors and/or for operation at low temperature, the carriers tunnel through a potential barrier if the barrier is sufficiently thin, induced by a large field [31]. The tunneling phenomenon is a majority carrier effect. Tunneling occurs either as field emission or thermionic field emission.

The Poole-Frenkel (PF) mechanism usually arises from the electric-field-assisted thermal excitation of charge carriers which originate from traps (charged and neutral) into the energy band of semiconductor. This internal emission transfers charges from potential traps at impurity levels to the conduction band. In PF effect, a net flow of electrons is caused by the reason of that electrons first neutralizing the trap will jump to the next trap. The current-voltage behavior and the barrier height are also given by equations (2.15) and (2.16), respectively. Where n= 2, η= 1, γ= 1, and the value of Φ_0 is being replaced by E_0, where E_0 is the trapping center energy in the dominance of PF emission [30].

Chapter Three
Experimental Details

3.1 Substrate cleaning

The glass substrates were rinsed using alcohol in order to remove dust and contaminants from the surface, followed by ultrasonic resonator in distilled water at 60 ℃ for 20 min. Then, the substrates were immersed in alcohol prior to deposition.

3.2 Thin film preparation

In this thesis, physical evaporation technique is used for the formation of the heterojunction structure. Germanium thin films were prepared at a vacuum pressure of 10^{-5} mbar. Ge powder was weighed (0.25 g) and placed in a tungsten boat (item 1 in figure 3.1) which is fixed inside the device. The glass substrates were located on the metal plate 20 cm above the source (item 2). There is a movable physical shutter control (item 3) above the evaporation source between it and the substrates used to avoid the random evaporation and to ensure uniform conditions throughout the whole duration of the deposition process. When the shutter is open, the substrates and the quartz crystal monitor are subjected to the deposition. When closed, the substrates are shielded from the deposition. The grown films thicknesses were about 200 nm. The thicknesses of the films were measured during evaporation by a crystal oscillator thickness monitors (item 4) that rely on the damping of an oscillating quartz crystal microbalance (QCM) through inertial loading to measure frequency shifts. QCM is used as the sensor. A thickness monitor measures how much material deposited on its sensor. The

sensor and the sample generally cannot be exactly in the same direction and position from the deposition source [32, 33].

.

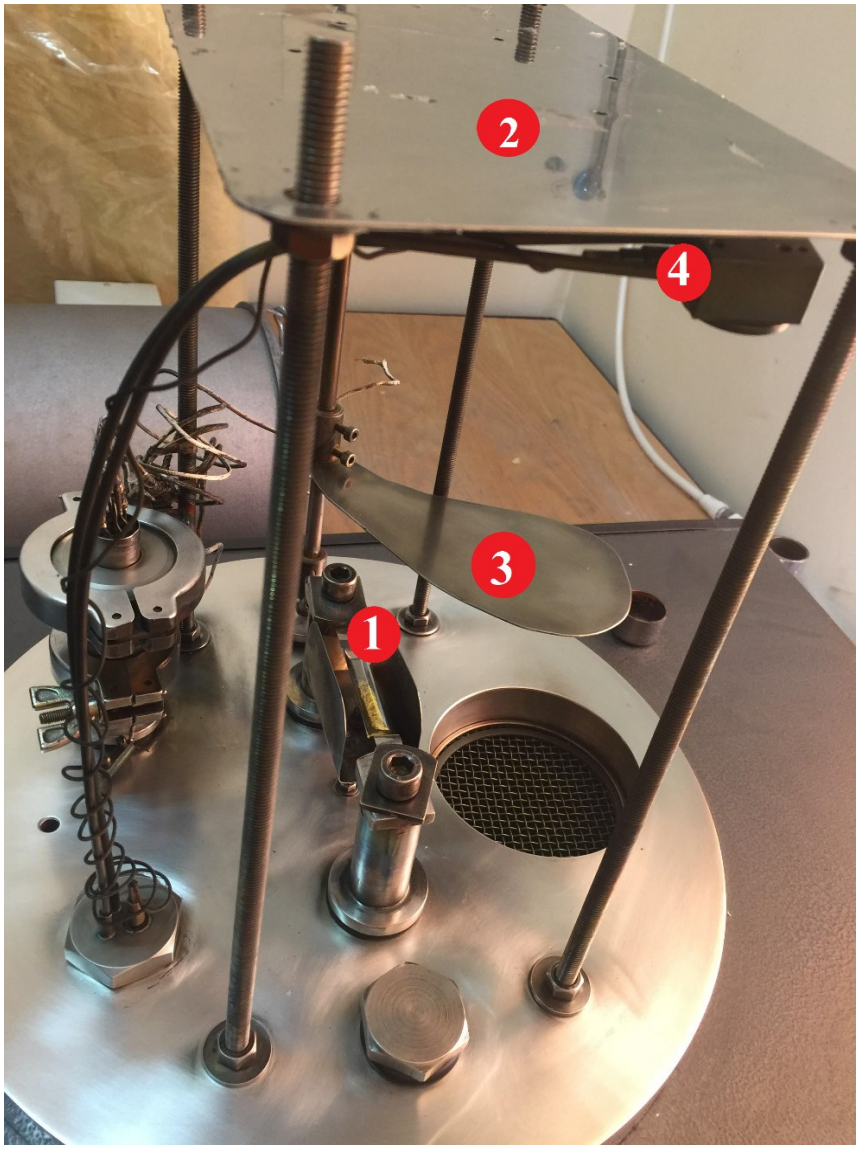

Fig. 3.1: The 600 VCM evaporation system.

During the evaporation process, one third of some Ge samples were covered by TEFLON stripe, the rest portion of samples were ready to execute the second run in evaporation system

for InSe deposition at the top of Ge layer and glass substrate. In this evaporation cycle, InSe was also deposited onto cleaned glass substrate. The thickness of the InSe was also 200 nm. In the third evaporation cycle, the half of the portion of the InSe surface was masked with TEFLON stripe to evaporate another 200 nm Ga_2S_3 at the top of Ge, InSe, and Ge/InSe films. The geometrical design of the samples are shown in the figure 3.2.

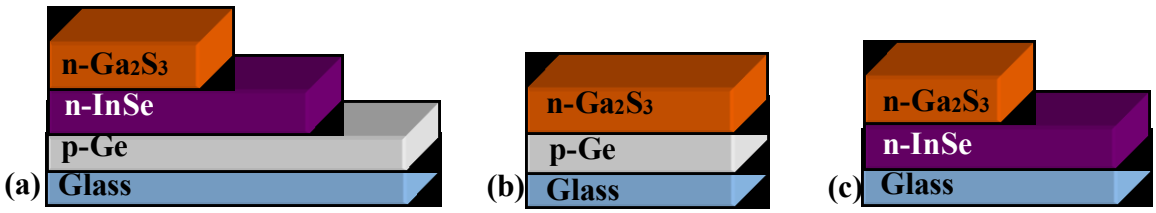

Fig. 3.2: The geometrical design of (a) Ge/InSe/Ga_2S_3, (b) Ge/Ga_2S_3, and (c) InSe/Ga_2S_3 heterojunctions.

For the electrical characterizations, the fabrication of Ge/InSe/Ga_2S_3 heterojunction requires the metal substrate instead of glass. Aluminum allows an electrical contact to the semiconductor the application of electrical fields. After getting Al/ Ge/InSe/Ga_2S_3 films, the Al and Au contacts were deposited onto the film surface to form ohmic/rectifying contacts using appropriate masks. The conductive carbon point contacts were deposited on the surface of the films.

3.3 Thin film analysis

The thin film analysis which are the sources of the scientific facts in this thesis are presented by means of structural, optical, electrical, and dielectric analysis in the fourth coming sections.

3.3.1 The "hot-probe" technique

The "hot-probe" technique which is shown in figure 3.3 was used in this work to distinguish between n-type and p-type Ge, InSe, and Ga_2S_3 semiconductors using a heater and a standard digital multi-meter (DMM). The hot iron is connected to the positive terminal of the multimeter while the cold one is connected to the negative terminal. A negative voltage was reading on the meter when the probes were applied to the Ge sample, indicating the p-type material. While InSe and Ga_2S_3 films yield positive voltages, indicating the n-type materials. An easy explanation for the hot probe results is that the carriers (electrons in an n-type, holes in a p-type) move within the semiconductor from the hot probe to the cold probe. The heat from the probe creates an increase in the number of higher energy carriers which then diffuse away from the contact point.

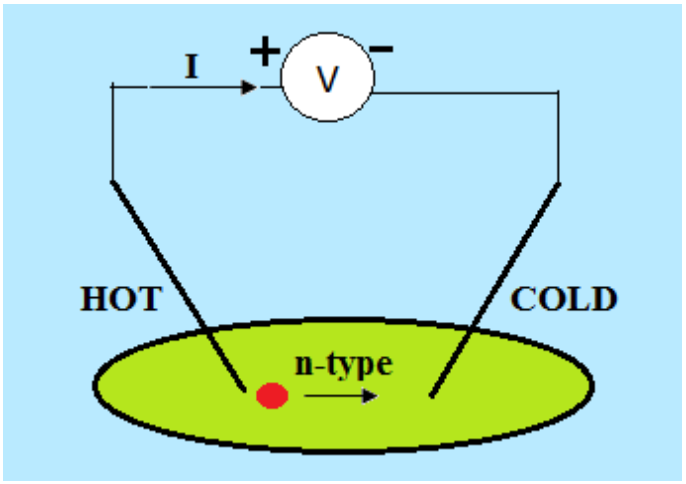

Fig. 3.3: Experimental set-up of the "hot-probe" experiment.

3.3.2 The x-ray diffraction (XRD) measurements

The Rigaku diffractometer equipped with K_α radiation of a copper anode of average wavelength 1.5405 Å at 40 KV and 15 mA were used to examine the lattice structure of

Ge/Ga_2S_3 and InSe/Ga_2S_3 interfaces. The 2θ step size was 0.1° and the scan rate was 5.0°/min. The system consists of a monochromator, a slit set, a detector and a sample holder. Figure 3.4 shows the schematic of an XRD system. Slits are used in order to adjust the size and shape of the x-ray beam. The sample moves by 2θ and the detector is counted the intensity through an angle 2θ. The sample is mounted onto the XRD holder using clay.

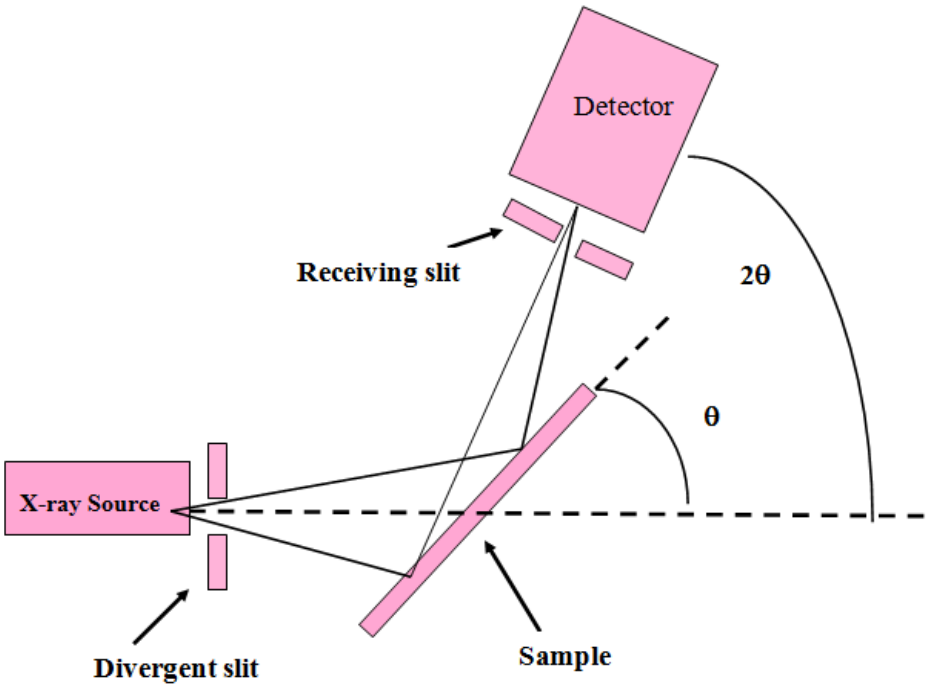

Fig. 3.4: Schematic of x- ray diffraction.

The data were collected in the 2θ range of 10-70°. The obtained XRD data were analyzed using TREOR-92 software package available in our lab.

3.3.3 Scanning Electron Microscopy (SEM) measurements

The scanning electron microscopy (SEM) with a Joel JSM 7600F instrument at King Abdulaziz University in Jaddah, is exploited to characterize the surface morphology of

deposited thin films. SEM technique involves a focused beam of electrons in order to scan the surface of the samples based on the principle that secondary electrons will be produced by inelastic collisions of energetic primary electrons, which are then ejected from a sample since they are attracted to a grid under low potential and then accelerated by a higher potential toward the detector. The field emission gun creates the primary electrons with energy range from few keV to 50 keV. While the secondary electrons have energies lower than that of the primary electrons by a factor of thousand. Thus, the electrons are emitted from a region that is a few angstroms from the surface of the sample. The emitted electrons signals are used to plot an x-y positioning in a form of matrix. Samples to be imaged, the beam is focused by a magnetic lens and then raster-scanned on a surface [34].

In particular, the SEM images with 30000 and 60000 enlargements were recorded for our samples.

3.3.4 Energy-dispersive X-ray spectroscopy (EDX)

The atomic content of the films was recorded by use of an energy-dispersive x-ray analyzer attached to the SEM system. In this technique, the composition of the sample elements is determined depending on the X-ray generation in which a unique set of characteristic x-ray for each element is produced and sorted depending on its energy. The system consists of x-ray generator e,g: semiconductor, solid-state detector, electronics and software. When the x-ray photon impinged the semiconductor, the electrons is knocked out from the semiconductor and produce a small current. The energy of the original x-ray can be calculated by measuring the current. Then, revealing a spectrum of the number of x-rays detected at each energy. From the spectrum, the weight of each element can be determined.

In our work, regions of 6 X 6 mm^2 were scanned and the ratios of In, Se, Ga and S atoms were determined.

3.3.5 Optical measurements

The optical transmittance and reflectance were measured in the incident light wavelength range of 300–1100 nm by means of a thermo- scientific Evolution 300 spectrophotometer that is equipped with VeeMax II spectrophotometer (figure 3.5). The reflectometer allows measurements at normal incidence (15°) and at variable angles in the range of 30-80° in 0.1° step.

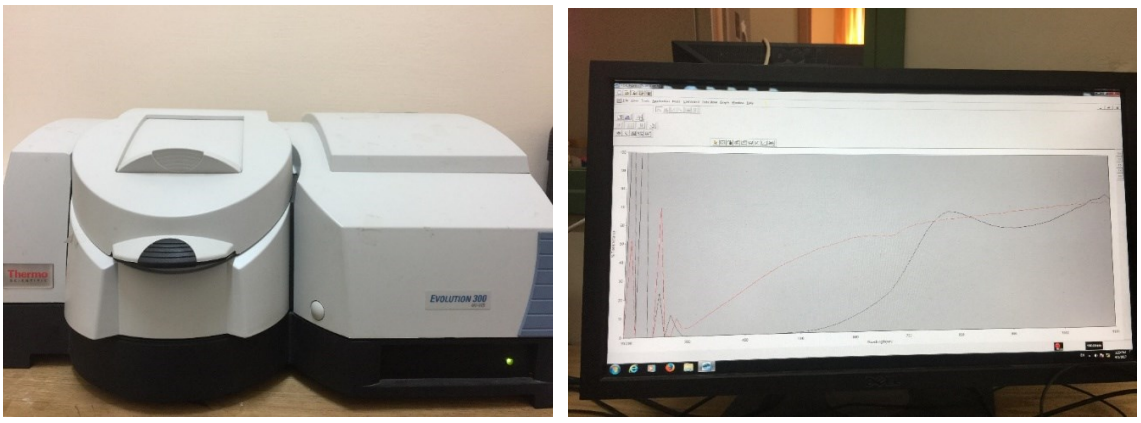

Fig. 3.5: The UV-VIS spectrophotometer.

The system includes an extended wavelength range from the UV to the near-IR silicon photodiode detectors. The data are collected and manipulated by means of the VISION software. The transmittance and reflectance measurements are employed to determine the optical band gap, materials absorbability, interband transitions and dielectric dispersion. The *T%* and *R%* measurements were carried out in the incident wavelength range of 300- 1100 nm.

3.3.6 Impedance Measurements

The ac signal was provided by Agilent 4291B RF Signal Generator impedance analyzer (10 MHz-1.8 GHz) spectrometer which is shown in figure 3.6. The device determines the total impedance (Z) that is composed of resistive and reactive parts. The reactive part is obtained through the measurement of the capacitance (C) and inductance (L). Since the capacitive part behaves as if a series and a parallel resistance are connected in the circuit, they are also measured.

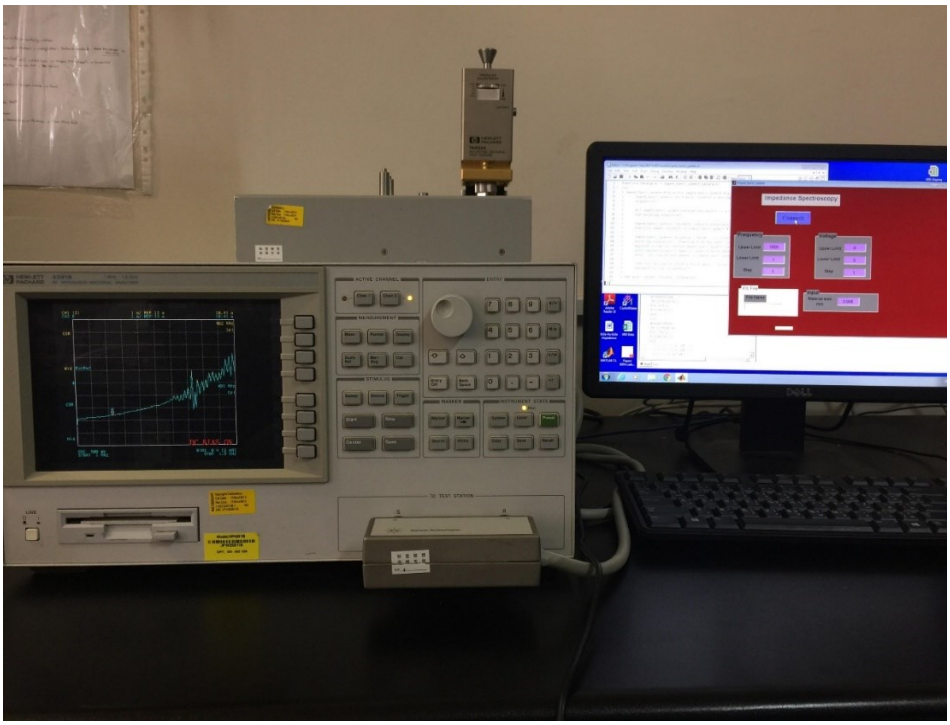

Fig. 3.6: Setup for impedance measurements including Agilent 4291B RF Signal Generator impedance analyzer.

The signal power was recorded with the help of MATLAB software. Remarkable characterization by measurements of output curves was performed with this device.

3.3.7 Current-Voltage Measurements

The current voltage (I-V) characteristics were registered between two Aluminum contacts as reference contact using computerized a Keithley 6485 picoammeter and a Keithley 230 voltage source in the dark. The Model 6485 Picoammeter has high sensitivity to measure currents less than 100 nA. Even at higher currents, this device makes accurate current measurements. It is also combined with functions like voltage, resistance, and charge measurement. The data were transferred using Keithley high-quality low-noise coaxial cables to reduce external effects. The I-V characteristic technique allows determining the relationship between the current flowing through an electronic device and the applied voltage across its terminals.

All the measurements were carried at room temperature in natural room atmosphere and the devices were not isolated from the environment.

Chapter Four
Results and Discussion

4.1 Structural Analysis

The InSe/Ga_2S_3 and Ge/Ga_2S_3 interfaces are subjected to compositional, morphological and structural analysis using EDX, SEM and X-ray diffraction techniques. EDX analysis on different regions of the InSe/Ga_2S_3 and Ge/Ga_2S_3 interfaces is shown in figure 4.1(a)-(c). In each EDX spectrum the Si, C, O, and K peaks are related to the glass substrate. The first region of energy dispersion X-ray analysis was taken over a 40.0 μm scale of enlargement on the Au substrate and InSe/Ga_2S_3 interfacing region. Figure 4.1(a) reveals an atomic content of 100% Au, 53% In, and 47% Se corresponding to a chemical formula of InSe. In various scanned points which are located at the middle of the sample, the atomic content of Ga and S was observed to be 41% and 59%, respectively, corresponding to correct formula of Ga_2S_3 in addition to the InSe phase as shown in figure 4.1(b).

The junction region between the Ge and the Ga_2S_3 is shown in figure 4.1(c) with 4.0 μm scale of enlargement, this region is found to be composed of 40% Ga and 60 % S indicates the chemical formula of Ga_2S_3.

The EDX results of atomic percentages has a main role for determining which type of conduction the films exhibit (n-type or p-type). In the case of Ga_2S_3, the excess S in the composition causes n-type conduction. The “hot probe” technique is used to determine the conduction type for our films as explained in section 3.3.1.

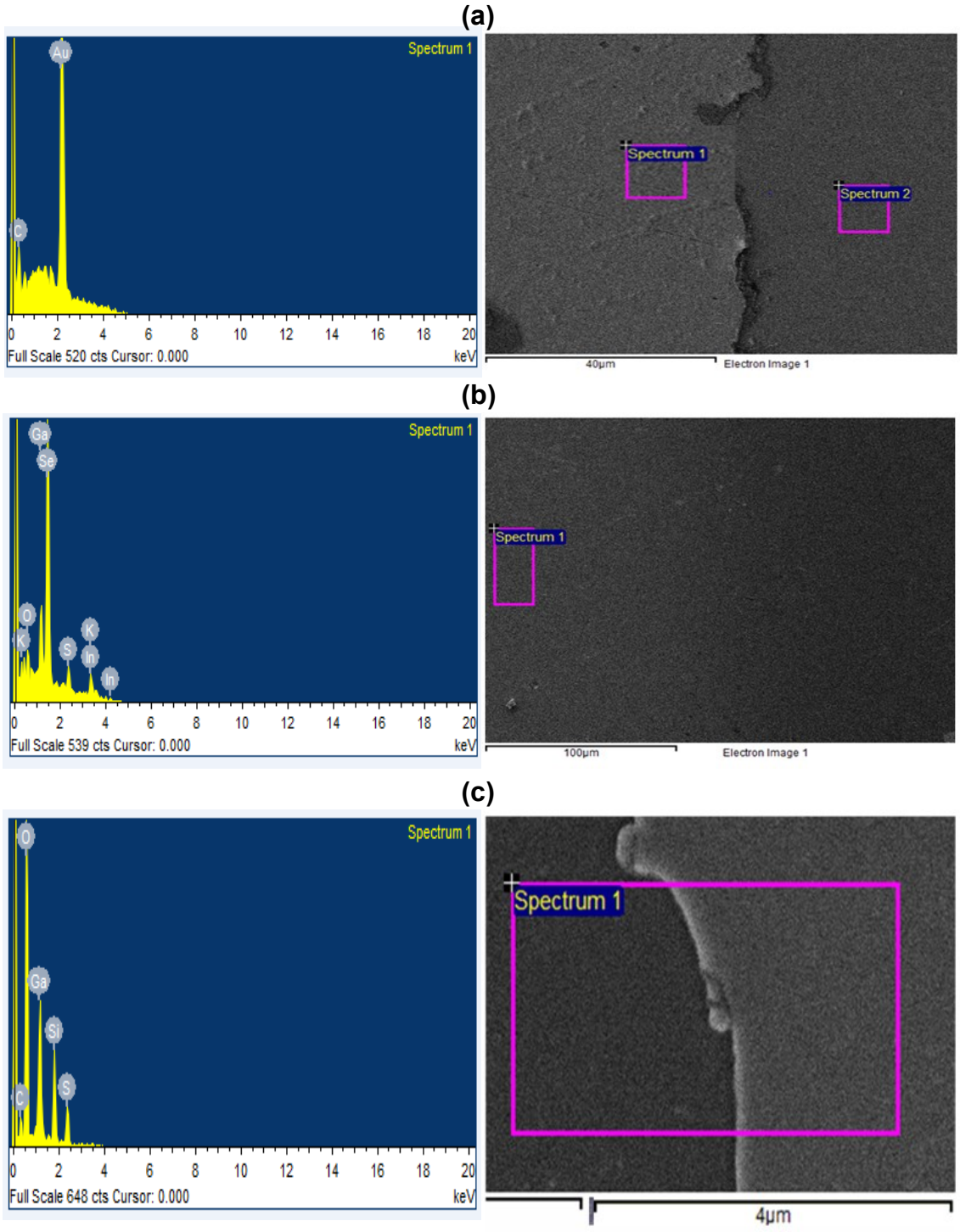

Fig. 4.1: The EDX spectra and images for (a) Ge, (b) $InSe/Ga_2S_3$ and (c) Ge/Ga_2S_3 films.

The SEM images which appear in figure 4.2(a)-(c) show that the Ge, InSe/Ga_2S_3, and Ge/Ga_2S_3 films are polycrystalline with distribution of grains forming semi-spherical shaped sheets. The Ge image displays in figure 4.2(a) which represented the 60,000 magnification of 6.0 scanned area of the film indicates that the large grains with an average size (D) of ~280 nm.

The InSe/Ga_2S_3 image displays distributed grains of average size of 175 nm as shown in figure 4.2(b). On the other hand, some grains in Ge/Ga_2S_3 image in figure 4.2(c) have average size of 50 nm.

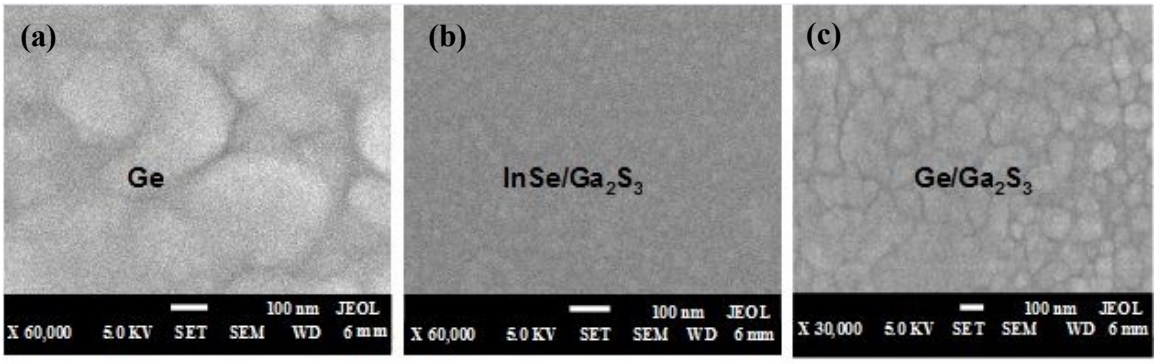

Fig. 4.2: The SEM images for (a) Ge, (b) InSe/Ga_2S_3 and (c) Ge/Ga_2S_3 films.

The results of the X-ray diffraction (XRD) that are presented in figure 4.3 were recorded for the Ge/Ga_2S_3 and InSe/Ga_2S_3 bilayers. The X-ray peaks were analyzed with the crystallographic 'TREOR 92' software, which allows the choice of the calculation method. It indexes the reflection lines with an expected cell and allows structural parameter expectations. As it is illustrated in the figure for Ge/Ga_2S_3 interface, a maximum peak that is best oriented in the (220) direction can be related to cubic Ge which exhibits lattice constant

5.65 Å [35]. In addition, the patterns also indicated another two main peaks that were found to be related to the cubic structure of Ge with preferable orientation in the (111) and (311), respectively. Minor peaks that appeared at 2θ = 66.1° and 73.1° are also assigned to the cubic Ge with (400) and (331) orientations, respectively. The XRD patterns of cubic Ge fit well with literature data [36].

Most of the other minor peaks are also assigned to monoclinic structured α-Ga_2S_3, which is a wurtzite based structure. The corresponding lattice constants of this phase are a= 11.094Å, b= 9.578Å, c= 6.395Å, and γ= 141.15° [37], α-phase has a crystal system characterized by three unequal axes at right angles. The α-term refers to the difference in the regular recurring state of the atoms. It is worth mentioning that the peak which appeared at 2θ = 27.5° may refer to (-312) α-Ga_2S_3 structure as reported in [12, 38]. A minor peak that appeared at 2θ = .600° was also assigned to the cubic structured Ga_2S_3 with lattice constant a= 5.17 Å [12]. On the other hand, According to the XRD results of GeS [39, 40], there is a possibility of chemical reaction that forms GeS at the Ge/Ga_2S_3 interface. This appears at angle of 2θ= 43.2° and 73.1°. The Miller indices of the recoded patterns are shown in the figure.

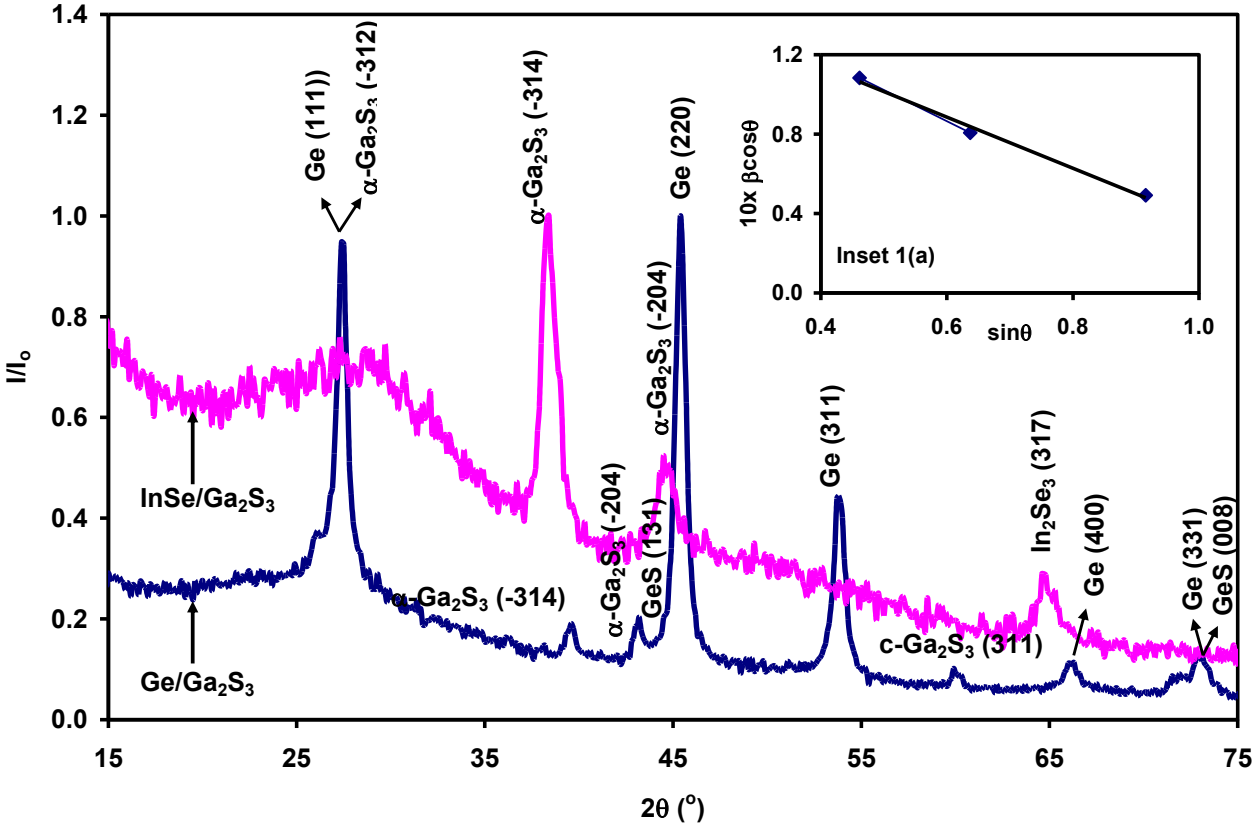

Fig. 4.3: The x-ray diffraction patterns for Ge/Ga_2S_3 and $InSe/Ga_2S_3$ films.

The XRD patterns of the Ga_2S_3 samples when they were deposited onto InSe instead of Ge are also represented in the same figure. All the α-Ga_2S_3 reflection peaks that appeared in Ge/Ga_2S_3 spectrum at 2θ= 39.7° and 43.2° with intensities 515 and 548, respectively, reappeared in $InSe/Ga_2S_3$ spectrum at 2θ= 38.4° and 44.5° with intensities 1038 and 544, respectively. The peak that appeared at 60.0° in Ge/Ga_2S_3 has disappeared in $InSe/Ga_2S_3$ spectrum. The shift in position of the peaks are also easily observed by comparing the Ge/Ga_2S_3 and $InSe/Ga_2S_3$ spectra. In addition, a minor peak appeared in the $InSe/Ga_2S_3$ spectrum at 2θ= 64.8°, which is related to γ-In_2Se_3 (317) orientation.

In order to understand the structural variations associated with the deposition of Ga_2S_3 onto Ge and InSe layers, detailed analysis of grain size (D) and strain (ε) was actualized using the combined expression for size broadening (Scherrer equation), which is presented in the first term of equation (2.2), and for the strain broadening expressions (Stokes and Wilson expression), through the second term of the equation (2.2) [41]. The values illustrated in table 4.1.

Table 4.1: The structural parameters of $InSe/Ga_2S_3$and Ge/Ga_2S_3 interfaces.

Spectrum	Ge/Ga_2S_3								$InSe/ Ga_2S_3$		
Peaks	Peaks of Ge					Peaks of Ga_2S_3			Peaks of In_2Se_3	Peaks of Ga_2S_3	
2θ (°)	27.5	45.4	53.8	66.3	73.1	39.7	43.2	60.0	64.8	38.4	44.7
Intensity (a.u.)	2546	2698	1199	306	356	515	548	253	298	1038	528
β (rad)	0.0122	0.0122	0.0139	0.0122	0.0174	0.0104	0.0069	0.0139	0.0192	0.0174	0.0209
sinθ	0.4615	0.7117	0.8067	0.9154	0.9566	0.6372	0.6843	0.86576	0.9046	0.6218	0.7031
cosθ	0.8871	0.7024	0.5909	0.4025	0.2913	0.7707	0.7292	0.50046	0.4263	0.7840	0.7110
(hkl)	(111)	(220)	(311)	(400)	(331)	(-314)	(-204)	(311)	(317)	(-314)	(-204)

The calculated *D* values are 85.7 Å and 321.7 Å for Ge/Ga_2S_3 and InSe/Ga_2S_3, respectively. The calculated strain values are 3.20x 10^{-3} and 3.67x 10^{-3} for Ge/Ga_2S_3 and InSe/Ga_2S_3, respectively. The strain value for Ge/Ga_2S_3 films has the negative sign (from the slope of inset 1(a)), indicating a compressive strain type in the structure [42]. It means that for a cubic unit cell of lattice parameter of 5.65 Å, the unit cell is compressed by 1.82%. The value of the compressing strain indicates that, the defects $\delta = 15\varepsilon/aD = 9.80 \times 10^{11}\ lines/cm^2$ in the Ge/Ga_2S_3 interface may also be ascribed to the defects that originate from germanium surface.

The lattice mismatches between Ge and Ga_2S_3 are calculated using lattice parameters and epitaxial relationship [31].

$$\Delta\% = \frac{a_e - a_s}{a_e} \times 100\% \qquad (4.1)$$

Where a_s is the lattice constant of the substrate and a_e is the lattice constant of the epitaxial layer. The lattice mismatches between a, b, c axes of monoclinic Ga_2S_3 and cubic Ge are 49.1%, 41.0%, 11.6%, respectively. The Ga_2S_3 and Ge cubic structures are closely lattice matched to each other (9.28%). In addition, the lattice mismatch between a-axis of hexagonal In_2S_3 and a-axis of monoclinic Ga_2S_3 was calculated to be 64%.

4.2 Optical Analysis

The spectral data of transmittance (*T*) for the Ge (200 nm thick), Ge/InSe (400 nm thick) and Ge/InSe/Ga_2S_3 (600 nm) films in the incident wavelength (λ) range of 300–1100 nm (270–

1000 THz) are presented in figure 4.4. As read from the figure, the transmittance of Ge thin films which are grown onto glass substrates slightly increased with increasing incident light wavelengths. The transmittance spectra for Ge/InSe and Ge/InSe/Ga_2S_3 are increasing in a wide range of light spectrum and the highest transition of 34 % and 59 % at λ of 670 and 880 nm, respectively. The *T%* values remain constant for all λ values greater than 880 nm.

When the glass substrate was replaced by transparent metal (Indium) substrate, the transmittance of In/Ge/InSe/Ga_2S_3 is approximately equal in value to that of three layer heterojunction for all $\lambda < 700$ nm indicating that the indium is transparent enough to keep the original transmittance unaltered. For $\lambda > 700$ nm, *T* becomes invariant with wavelength and exhibit maximum *T%* of 50%. The decrease of *T%* by existence of In may be assigned to low transparency of indium near the IR region [43].

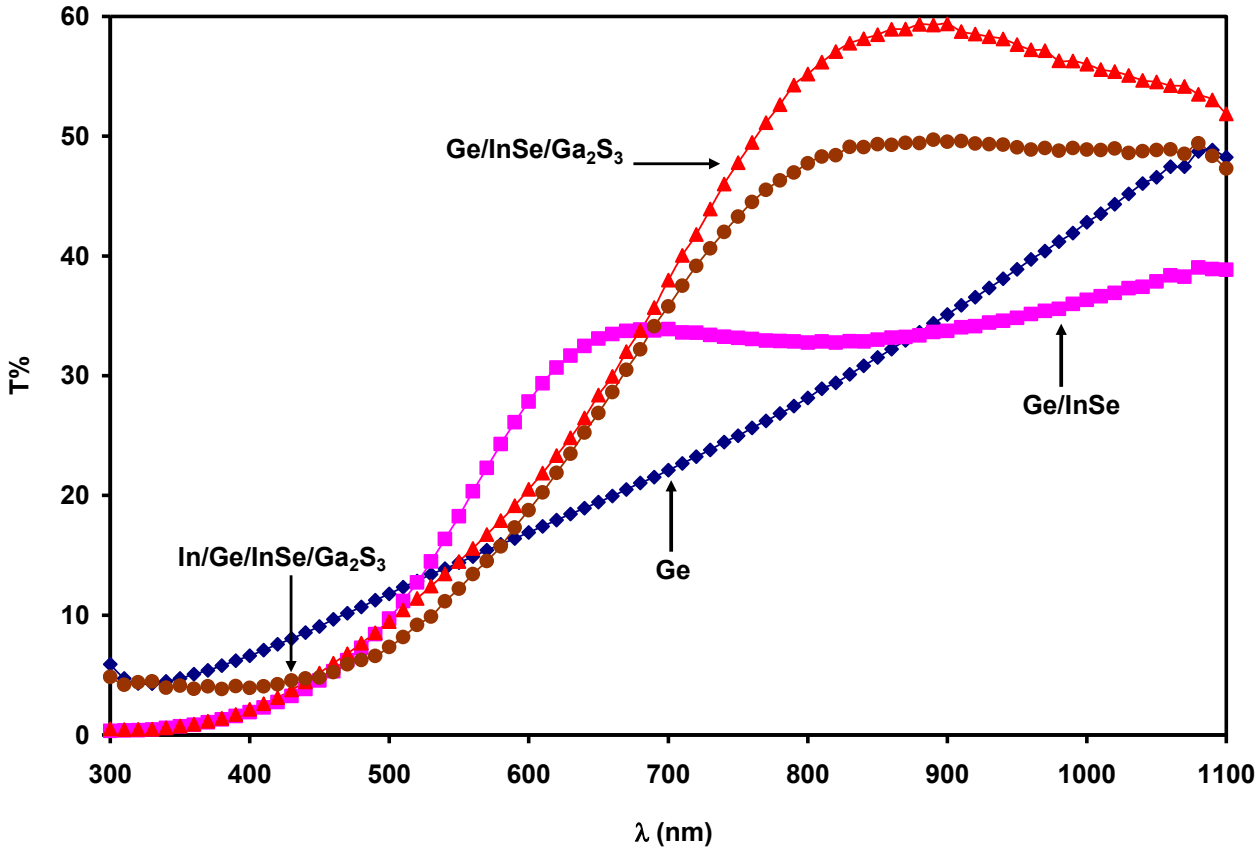

Fig. 4.4: The transmittance spectra for Ge, Ge/InSe, Ge/InSe/Ga_2S_3, and In/Ge/InSe/Ga_2S_3 interfaces, respectively in the range of 300-1100 nm.

On the other hand, the reflectance (*R*) spectrum of Ge layer slowly increases with increasing light wavelength. The spectrum of Ge/InSe deceases with increasing the light wavelength for all $\lambda < 580$ nm. Above this value of λ, *R* starts to increase and crosses the *R* spectrum of Ge at 940 nm. Moreover, the *R*-λ spectrum for Ge/InSe/Ga_2S_3 exhibits some interference patterns with maximum *R%* value at $\lambda = 364$ and 600 nm. It also showed a minimum reflectance value of 3.0% at $\lambda = 800$ nm. It is also readable that in contrast to the behavior of the transmittance spectra, the *R%* values of the Ge/InSe/Ga_2S_3 interface become much less than that of Ge/InSe above 670 nm.

However, if the three layers deposited on In substrate are considered, the first interference pattern disappeared and the amplitude of the second lowers by nearly 15%, the minimum reflection shifted toward visible light region as shown in figure 4.5.

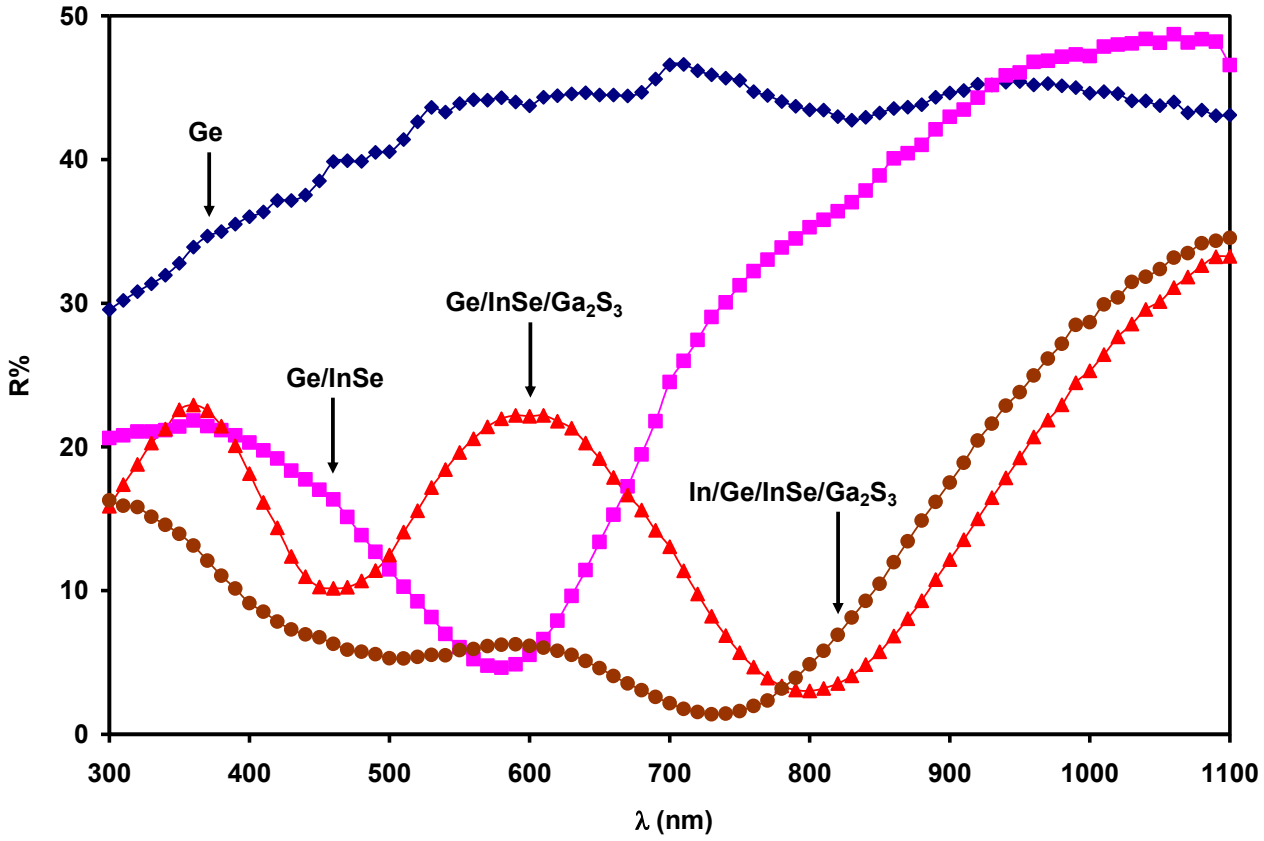

Fig. 4.5: The reflectance spectra of Ge, Ge/InSe, Ge/InSe/Ga_2S_3, and In/Ge/InSe/Ga_2S_3 heterojunctions, respectively in the range of 300-1100 nm.

Extinction of the transmission and reflection of a material improves absorbance (A). Such properties are obtained by design of an appropriate structure in order to achieve high absorbance at a particular frequency. The optical absorbance was found from the measured R and T by the equation $A\%=100\%–T\%–R\%$ [44]. The absorbance curves in figure 4.6

reflected a complementary picture for the light dynamics on the films surfaces. For all films the absorbance never reaches zero value suggesting the existence of interband transitions. The interband processes relate to transition of electrons and holes from band to band through the energy band gap [43].

These transitions may be ascribed to the existence of the defects that introduces alternative energy levels between the intrinsic bands and, thus, subsequently reduces the band gap [45]. This process is ascribed to the electric field caused by the externally added charge (the free moving charges) and the internally induced charge (the bound charges), the electron–phonon interactions and the scattering of electron at interfaces [43].

As the figure also illustrates, the absorbance spectra for the Ge monolayer and the Ge/InSe bilayers indicated an improvement in the absorbing ability of Ge as a result of the InSe window covering in the IR region. The absorbance of Ge films which are grown onto glass substrates decreases as the wavelength increases and has an absorption shoulder at about 700 nm which isn't shifted when adding InSe. The data indicated a significant increase in *A%* when the interface is designed. The Ge/InSe bilayer films show three regions of variations; it starts with constant absorbance level up to 500 nm. It then sharply decays in the incident light wavelength range of 500–700 nm. The curves move slowly decreasing for $\lambda > 700$ nm. However, by deposition of Ga_2S_3 layer, the shoulder has low shift toward UV region. In addition, one may observe the remarkable increase in the absorbability of the Ge/InSe/Ga_2S_3 upon replacement of glass with In film, the shoulder disappeared and the absorbance is approximately linearly decaying.

Similar enhancement in the amount of absorption had been obtained by growth of TiO_x on the PCDTBT co-polymer substrates that is reported to increase the absorbance of the heterojunction and increase the internal quantum efficiency of the device up to 100% [46].

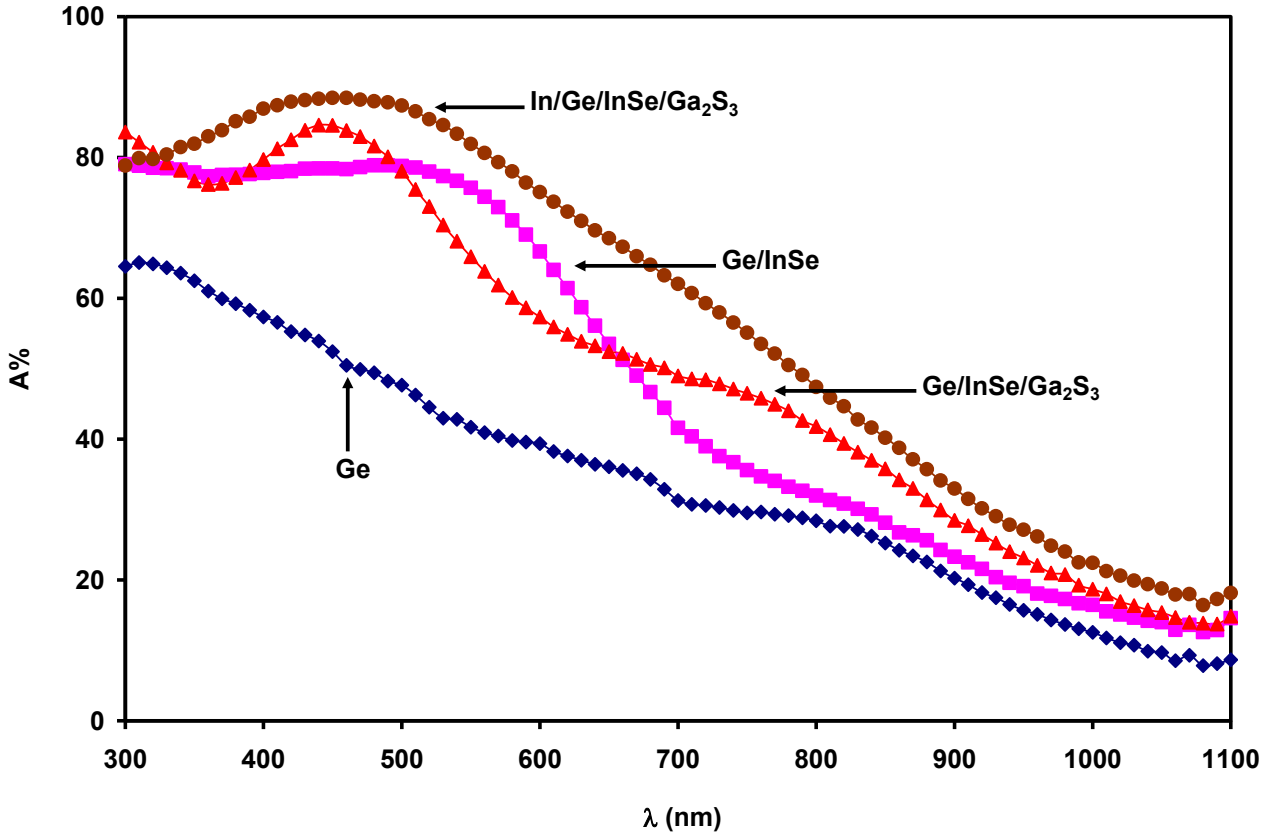

Fig. 4.6: The optical absorbance being recorded in the incident photon energy range of 1.1–4.2 eV for the Ge, Ge/InSe, Ge/InSe/Ga_2S_3 thin films.

To optimize more informative knowledge about the optical properties of the Ge/InSe/Ga_2S_3 system, the energy band splittings between the conduction and valence band of the glass/Ge, Ge/InSe and Ge/InSe/Ga_2S_3 films are investigated. For this purpose, the absorption coefficients (α) for the films under studying were determined from the relationship ($\alpha = A/d$, d: thickness) [47]. The absorption coefficient (α) is a key parameter to design an

optoelectronic device. In the case of solar cells, by decreasing the reflection of incident light, increasing the optical intensity and optical path of the material, the effective absorption can be increased [48].

The relation between the absorption coefficient (α) and the incident photon energy (E) is represented in figure 4.7. It is found that the absorption coefficient has the same behavior like that of the absorbance; however, the absorption coefficient provides information about light penetration depth into the layers. It is clearly observed that the sharp increase in the absorption coefficient of Ge layer with increasing energy above 1.5 eV is followed by smooth variation in the remaining region of absorption. In contrast to this behavior, for the double and triple layers heterojunction, the variation of absorption coefficient with incident photon energy terminates for all light spectrum above 2.2 eV. Such behavior can be assigned to the higher thickness of the films when the Ga_2S_3 was deposited at the top of Ge/InSe films. In addition to the large lattice mismatch between the optical layers as mentioned through the x-ray analysis. Indium metal makes the same behavior of three layers heterojunction that lack In substrate with little sift in absorption edge.

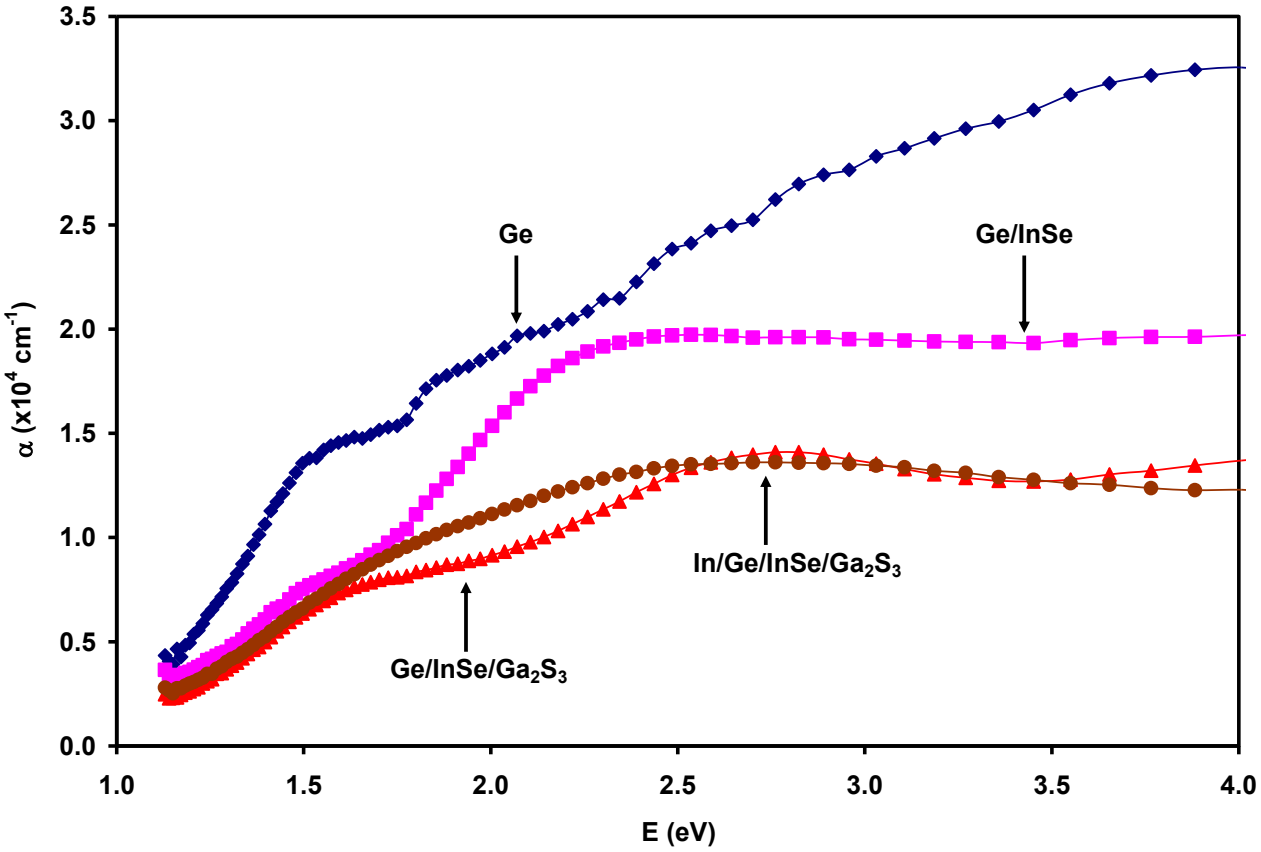

Fig. 4.7: The absorption coefficient (α) as a function of photon energy in the range of 1.0 to 4.0 eV.

The calculated absorption coefficient (α) spectrum is used to obtain the changes in the energy band gap of the Ge as a result of interfacing. The optimization of the energy band gap is based on the usual fitting procedure of determining the value of the band gap in which the Tauc's relation (2.5) is employed [21]. To apply this relation for the samples under study, $(\alpha E)^{1/2}$, $(\alpha E)^2$, $(\alpha E)^{1/3}$ and $(\alpha E)^{2/3}$-E dependence has been plotted in figure 4.8(a)-(d) and evaluated for indirect allowed, direct allowed, indirect forbidden and direct forbidden electronic transitions, respectively. If an appropriate value of p is used to obtain a linear plot, the intercept on the E-axis should give the value of the energy band gap (Eg). It is found to be best fit that linearly include the widest range of data for an exponent values of p = 1/2 and

2. Thus, as appears in figure 4.8, the dominant energy band gap in the Ge based heterojunction relate to the indirect and direct allowed transitions. From the respective E-axis crossing of the plots. The fitting procedures in these plots are carried out by using a special high-convergence minimization technique which makes use of regression and residual sums of (R^2) coefficient of determination and residual mean squares statistical analysis. All the fits were restricted to give a residual sum of R^2 equals or greater than 0.025. In accordance with this statistical approach, the p= 1/3 and p= 2/3 values should be excluded. The $(\alpha E)^{1/2}$ and $(\alpha E)^2$ -E variation covers the widest range of data as shown in figure 4.8(a)-(b).

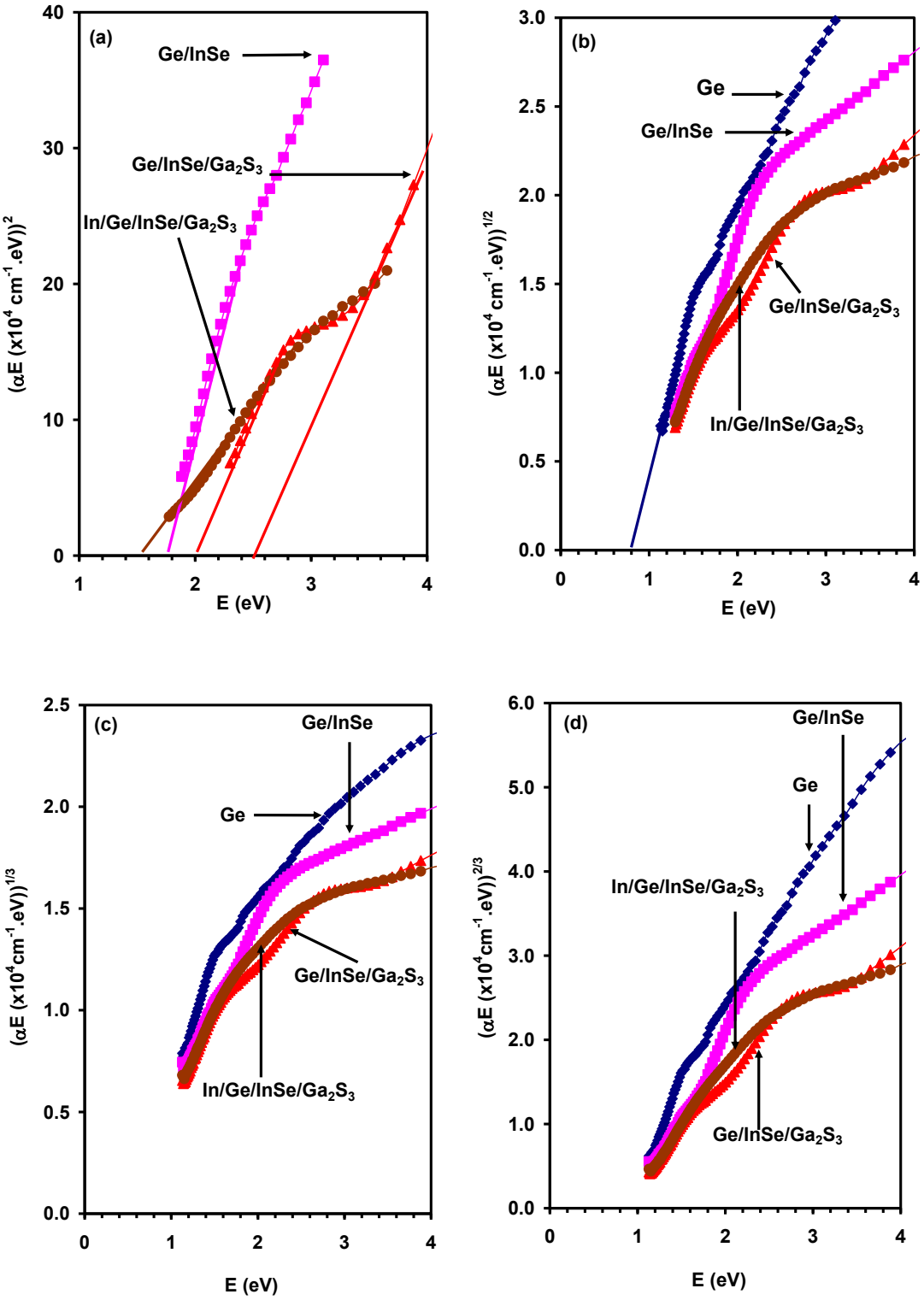

Fig. 4.8: The $(\alpha E)^{1/p} - E$ variation for Ge, Ge/InSe, Ge/InSe/Ga_2S_3 and Ge/InSe/Ga_2S_3 films for (a) p=1/2, (b) p= 2, (c) p= 3, and (d) p= 3/2.

The straight solid line which crosses the energy E-axis reveals an indirect allowed energy gap of the Ge samples is 0.80 eV, which is close to the value being for Ge 0.73 eV [49]. The direct energy band gap value shifted to 1.77 eV when the Ge was covered by InSe. The energy band gap of the Ge/InSe thin film increases from 1.77 eV to 2.00 eV (E_{g1}) and to 2.50 eV (E_{g2}), when joined to a Ga_2S_3 layer. The energy band gap differences between that of Ge/InSe and those of Ge/InSe/Ga_2S_3 interface are ΔE_{g1} = 0.23 eV and ΔE_{g2} = 0.73 eV, respectively. Since the electron affinity ($q\chi$) of InSe is 4.55 eV [50, 51] and that of Ge is 4.13 eV [31], then the conduction band offset $\Delta E_C = (q\chi_{InSe} - q\chi_{Ge}) = 0.42\ eV$. This leads to a respective valence band offset of $\Delta E_V = (E_g - \Delta E_C) = 1.35\ eV$. The reason for the valence band discontinuity is the interface charge dipole and electron–hole recombination at the depletion layer boundaries [52]. This value of ΔE_V (valence band shift) is attractive for design of Schottky barrier optoelectronic devices. It is also applicable in devices that require strong carrier confinement such as thin film transistors since sufficiently large valence band offset between the active layer and the dielectric in order to avoid high leakage current [53]. The difference between the theoretical data in literature [4, 37] and the currently reported data is assigned to some factors like low crystal symmetry, large lattice mismatches and plane orientation dependencies. On the experimental side, such conditions could cause a stronger confinement of the charge carriers at the interfaces. The excitons effect is become more apparent by this confinement [54, 55]. The presented valance band offset values for the Ge/InSe/Ga_2S_3 interfacing which is equal 1.25 eV are promising as they guarantee the success of this interface to use in optoelectronic devices and thin film transistors [56, 57]. When the heterojunction is made on indium the energy band gap decreased to 1.57 eV due

to the band bending mechanism caused by the probable Schottky barrier formation at In/Ge side. The Schottky barrier forms because the work function of indium being (4.12 eV) is less than that of p-Ge (5.02 eV) [2, 31, 58], the energy band gap shift (ΔEg) at the interface being 0.23 eV is sufficient to design a point contact devices such as Schottky solar cells and narrow barrier resonant tunneling diodes [59].

This shift in energy gap upon materials interfacing is usually attributed to lattice mismatches and defects. The latter is assigned to impurities and incomplete bonds at the interface of the heterojunctions [3, 60], the lattice mismatch forces the valence electrons to exist in two different spaces that leads to the shift in Eg, In addition, the dipole layer at the interface could play significant role. The dipole layer appears as a result of the tunneling of electron from the conduction band of one material into the Eg of the other material [61, 62].

Table 4.2: Energy band gap value for the heterojunctions

	Ge	Ge/InSe	Ge/InSe/Ga_2S_3	In/Ge/InSe/Ga_2S_3
E_g (eV)	0.80	1.77	2.00/ 2.50	1.57

To extend the applications possibilities of this structure we now turn the attention to the dielectric properties of the Ge interface construction. Figure 4.9 and figure 4.10 shows the dielectric spectra of the Ge, Ge/InSe, Ge/InSe/Ga_2S_3 and In/Ge/InSe/Ga_2S_3 interfaces determined from the reflectance data which were displayed in figure 4.5. The effective dielectric constant (ε_{eff}) is determined from the equation [21]:

$$R = \frac{\left(\sqrt{\varepsilon_{eff}}-1\right)^2+k^2}{\left(\sqrt{\varepsilon_{eff}}+1\right)^2+k^2} \qquad (4.2)$$

In order to visualize detailed information about optical signal quality and dispersion, the real (ε_r) part is: $\varepsilon_r = \varepsilon_{eff} - k^2$ [63] and imaginary (ε_{im}) part is: $\varepsilon_{im} = 2\sqrt{\varepsilon_{eff}}k$ [64], and the components of the effective dielectric constant, $\varepsilon_{eff} = \varepsilon_r + i\varepsilon_{im}$ are also determined. Both are related to the extinction coefficient (k), with $k = {a\lambda}/{4\pi}$. The decrease or increase in k value affects the regions where the reflection increases or decreases.

The respective spectra of real and imaginary parts of the dielectric constants are shown in fig. 4.9 and figure 4.10, respectively. The interface exhibit very interesting dielectric spectra. Namely, the real part of the dielectric constant of monolayer slightly decreases with increasing incident light frequency (F). The peak which appeared at 425 THz (2.8 eV) can ascribed to well oriented dipoles that increases the dielectric constant; It coincides with the excitonic indirect energy band gap of Ge films that results from the transitions between Γ_7 and Γ_8 points in the 1st Birllouin zone [37]. For the bilayer, the real dielectric constant sharply decreases reaching a minima at 510 THz. The ε_r of bilayer follows a linear equation presented by $\varepsilon_r = -0.1494F + 73.028$. This indicates a good dipole polarization associated with high dielectric constant value in the IR region of light. It then increases with increasing frequency till reaches 800 THz, where it tends to be constant with increasing frequency. The dielectric constant of Ge/InSe/Ga_2S_3 samples continuously decreased with increasing frequency. The increase in the dielectric constant up to 495 THz which is followed by a decreasing with minimum peak at 655 THz. Where it tends to re-increase with increasing frequency reaching a maxima at 828 THz and then returning to decrease. When Ge/InSe/Ga_2S_3 was deposited on indium substrate, the real dielectric constant is higher than that of the interface without In

substrate in 300-383 THz. The existence of indium layer supplies more surface electrons that couple with Ge holes or ion cores resulting in higher values of ε_r.

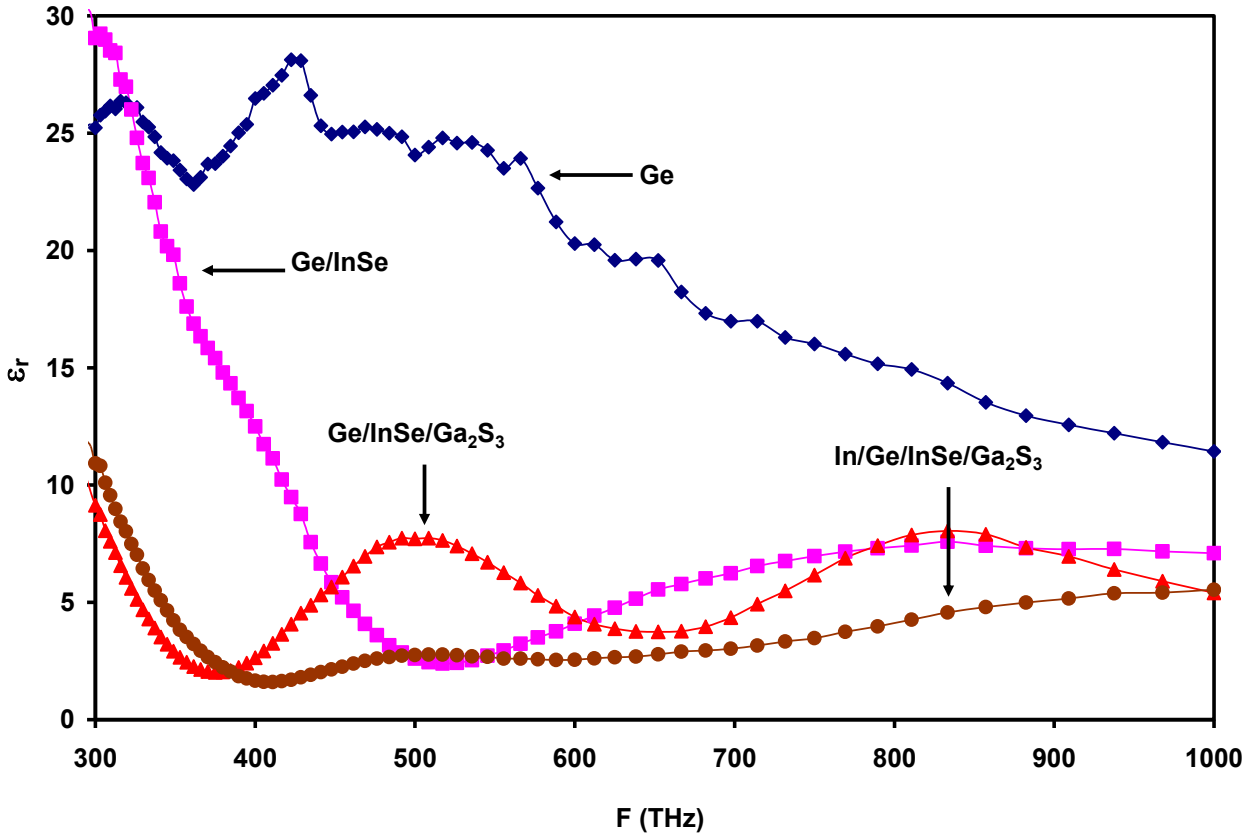

Fig. 4.9: The real dielectric constant for Ge, Ge/InSe, Ge/InSe/Ga_2S_3, and In/Ge/InSe/Ga_2S_3 interfaces in the range of 300-1000 THz.

On the other hand, the imaginary part of dielectric spectra which appears in Fig. 4.10 illustrated that for Ge films, values are relatively low compared to ε_r, ε_{im} increases with increasing frequency and reach maximum value at 443 THz.

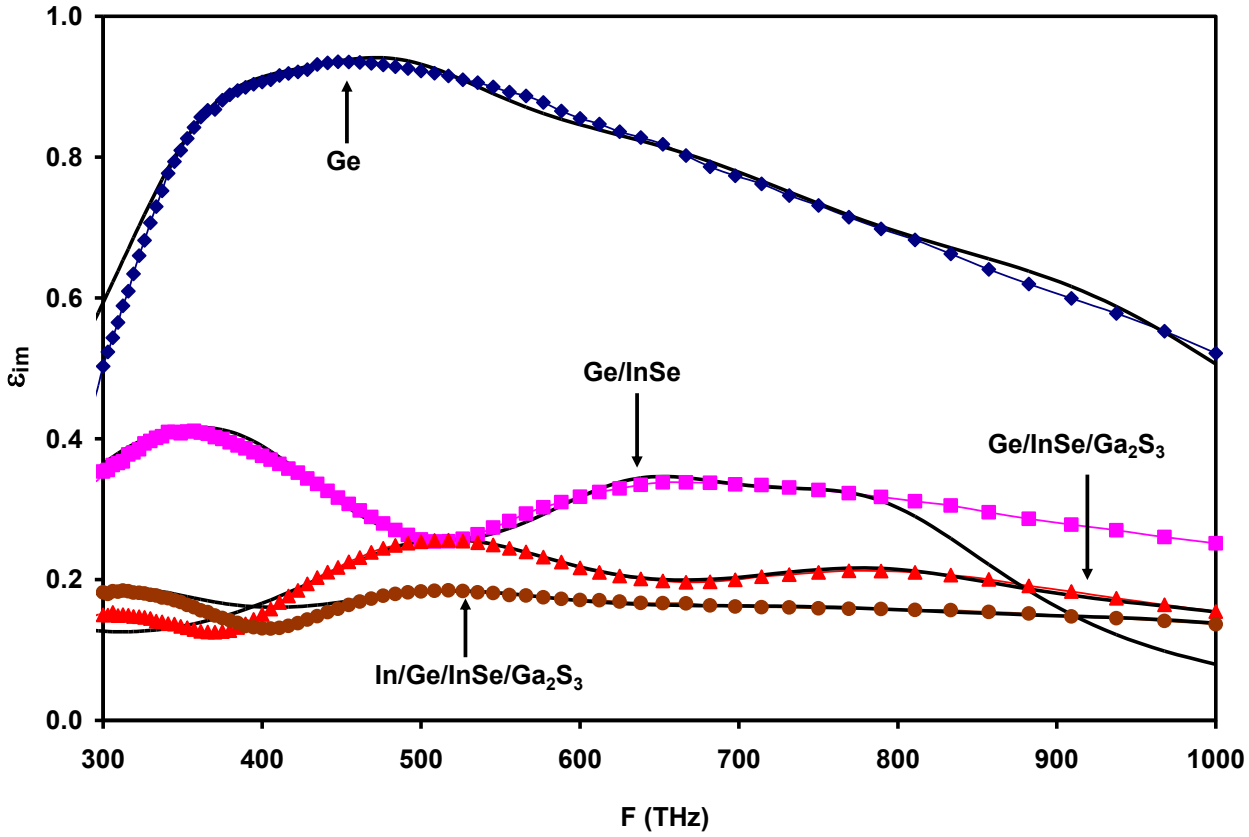

Fig. 4.10: The imaginary dielectric constant for Ge, Ge/InSe, Ge/InSe/Ga_2S_3, and In/Ge/InSe/Ga_2S_3 interfaces in the range of 300-1000 THz.

The variation of the imaginary part of the dielectric constant was modeled in accordance with the Drude-Lorentz model which connects the imaginary part of dielectric constant with incident light frequency through the modified relation [64]:

$$\varepsilon_{im} = \sum_{i=1}^{K} \frac{{w_{pe_i}}^2 w}{(({w_{ei}}^2 - w^2)^2 + {w_i}^2 {\tau_i}^{-2})} \qquad (4.3)$$

Where k is number of observed peaks. In our work, k= 4. τ is the electrons scattering time. The experimental data was reproduced again by substituting the reduced effective mass $m*$ = $((m_e(\text{Ge}))^{-1} + (m_e(\text{InSe}))^{-1} + (m_e(Ga_2S_3))^{-1})^{-1}$ for the Ge/InSe/Ga_2S_3, m* = 0.280, 0.095,

0.077, and 0.0713m_0 for Ge, Ge/InSe, Ge/InSe/Ga_2S_3 , and In/Ge/InSe/Ga_2S_3, respectively. Where m_h(Ge) = 0.28m_0 [65], m_e(InSe) = 0.143m_0 [66], m_e(Ga_2S_3) = 0.4m_0 and m_e(In) = 1.04m_0 [13]. In addition, the values of τ_i, w_e, n, and μ are estimated with the help of equation (4.3). μ is the frequency dependent drift mobility, $\mu = e\tau/m^*$. The results are tabulated in Table 4.3. The obtained complete solution illustrated by the black-colored line in figure 4.10. The fitting procedure indicates pronounced typical coupled oscillator set that are subjected to resistive forces that lead to damping rate of $\gamma = \tau^{-1}$. The collision of photoexcited carriers with impurities, phonons and other carriers are sources of the damping [64].

The tabulated data indicates that, the resulting reduced resonant frequency (w_e) which takes into account the effects of the interband transitions (local fields) on the dielectric function is continuously increasing with increasing incident light frequency and increasing the layers of heterojunction. Moreover, the electron bounded plasma frequency (w_{pe}) which is depending on the number of free electrons (n), exhibits the same behavior i.e increases with increasing frequency. The number of free electrons increases in each film causing an increase in the value of w_{pe}. It is observed that, the number of free electrons in Ge films is higher than that of bilayer. The more free electrons in Ge is assigned to the narrower energy band gap of Ge which make electrons transfer more energy. Further increase in the thickness by deposition of Ga_2S_3, gives the smaller (n). As a result the drift mobility falls. This fall is associated with remarkable increase in the electron bounded plasma frequency and is also ascribed to the increase in the damping rate γ. Moreover, in the presence of indium substrate, the relaxation time is lower than that of Ge/InSe/Ga_2S_3, meaning the increase in damping and electronic friction for the device. The decrease in the density of free carriers may cause by the fact that

when the p-type Ge layer deposited onto In substrate, the number of majority carrier decreases. We should consider that the 200 nm of Ge is large compared to 50 nm In and has high roughness that leads to short circuit

Table 4.3: The fitting parameters of Drude model for the Ge based heterojunctions.

	Ge				Ge/InSe				Ge/InSe/ Ga_2S_3				In/Ge/InSe/ Ga_2S_3			
$\tau_i(fs)$	0.80	0.63	0.35	0.32	0.83	0.79	0.70	0.65	1.20	0.60	0.50	0.37	0.85	0.60	0.34	0.32
w_{ei}(x$10^{15}Hz$)	2.35	3.10	4.30	6.00	2.00	2.50	4.05	5.00	0.90	3.30	5.00	6.50	2.00	3.30	4.80	6.50
n (x 10^{17} cm^{-3})	88.0	130	400	490	11.0	18.0	29.0	40.0	7.00	21.0	25.5	32.0	5.50	9.50	22.5	33.0
$\mu(cm^2/Vs)$	5.02	3.97	2.20	2.01	15.4	14.6	12.9	12.0	27.4	13.7	11.4	8.45	21.0	14.8	8.38	7.89
w_{pei} (GHz)	3.33	4.05	7.10	7.86	2.02	2.59	3.28	3.85	1.79	3.10	3.42	3.83	1.65	2.17	3.34	4.04

4.3 Impedance Spectroscopy

The impedance spectroscopy which is regarded as a powerful tool to explore the ac signal processing mechanism through samples is employed in the spectral range to 10-1800 MHz. When the ac signal is applied to the device, the capacitance (*C)* of the device which is shown in figure 4.11 displayed a resonance (series) and antiresonance (parallel) behavior. As it is easily readable from the figure, which presented the capacitance for Al/Ge/InSe/Ga_2S_3/ (Au, C, and Al) contacts (pnn interface), the series frequency (f_s) appears at 163 and 172 MHz and the parallel resonance (f_p) appears at 173 and 181 MHz for devices contacted with C and Al, respectively. The antiresonant frequency for Al/pnn/Au is 19 MHz while the series resonance frequency is beyond the region of measurement for devices of Au contact. The capacitance values are negative for the last mentioned contact in the spectral range less than 200 MHz. In general, the negative capacitance is caused by injection of minority carriers (tunneling) at forward bias. This property is used to the cancellation of positive capacitance in altering the signal properties of resonant electronic circuits especially in time-based sensor interfaces to control the oscillation with enhanced tuning and to increase the tuning range of voltage-controlled oscillators (VCOs) with minimal phase noise or power impact [62, 67-69].

The capacitance values of the Al/pnn/Au contain external resonance peaks which exhibit maxima at 1332, 1369 and 1409 MHz and aniresonance at 1343, 1389 and 1442 MHz. Maximum capacitance value is 1.2 nF (inset 2(a)). The value is of less importance compared with the main peaks that appear at 163 MHz and 172 MHz with amplification of 8.54 nF and 8.26 nF, respectively. Further increase in the applied frequency did not change the capacitance value.

The resonance peaks apparent in the C–f spectra could be explained by taking into account the number of electrical dipoles, which can orient with the external oscillating electric field in a shorter period of time increases with increasing ac signal frequency. As a result, the number of free charges available for conduction decreases and the dielectric constant increases. The increase in dielectric constant causes an increase in the electric flux density since it reflects the extent to which the material concentrates electrostatic lines of flux. This process keeps until the time needed for the dipole orientation is equal to the ac signal time, at which the maximum resonance peak appears. For larger frequency values (shorter ac signal times), the oriented dipole with the applied signal reduces and the dielectric constant decreases. This process continues until the dipole do not feel the changes of applied oscillating electric field, which means reaching a fixed dielectric constant and thus fixed capacitance [70].

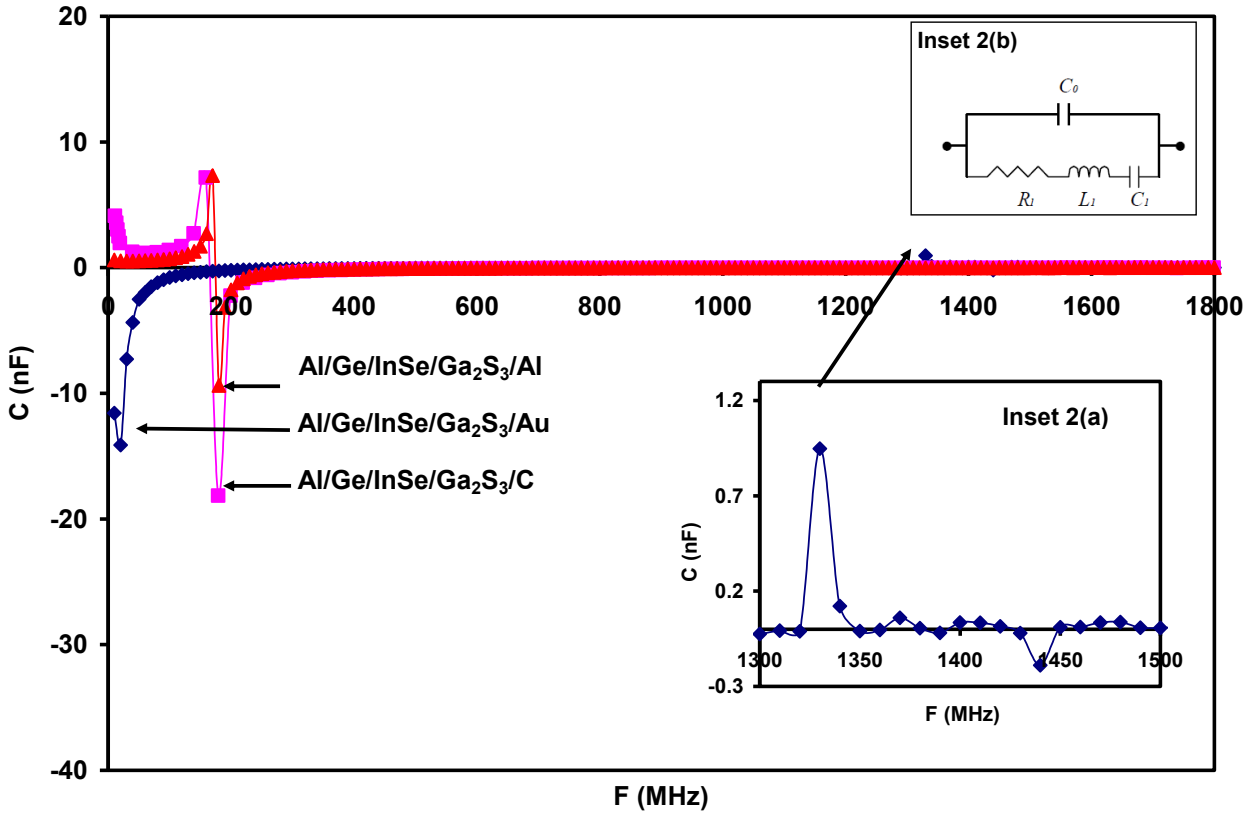

Fig. 4.11: The results of the ac signal analysis for the capacitance of pnn heterojunction being recorded at zero bias voltage in the frequency range of 1.0MHz-1.8 GHz.

The bandwidth of the resonance– antiresonance peaks of pnn heterojunction is presented by the frequency difference $\Delta f = |f_p - f_s|$, which is about 10 MHz. This value is important since it presents that the number of data transfer cycles could reach 10 million per second without any distortion. This nominate the devices for use as fast electronic switches that alter state in a period of time $(1/\Delta f) \sim 10^{-7}$ s and as microwave resonators attractive for communication technologies [69, 71].

The data shown in figure 4.12 (a)-(b) related to the measured values of resistance (R), inductive ($X_L = \omega L$) and capacitive ($X_C = {}^{1}/_{\omega C}$) reactance. The impedance which is the opposition to current flow in ac circuit, is made up of these three components [24] $Z = \sqrt{R^2 + (X_L - X_C)^2}$ consistently, one may observe from figure 4.12(a) and (b) that the resistance and impedance increase with increasing applied frequency.

Moreover, it is worth mentioning that the spectra of both Z and R arranged in accordance to the work function of the metals (Au, C, and Al). The Z and R are higher for metals with higher work function. This is because the energy required for electrons to transmit is large. This facilitates the electronic transportation at the metal semiconductor interfaces so the resistance decreases [24].

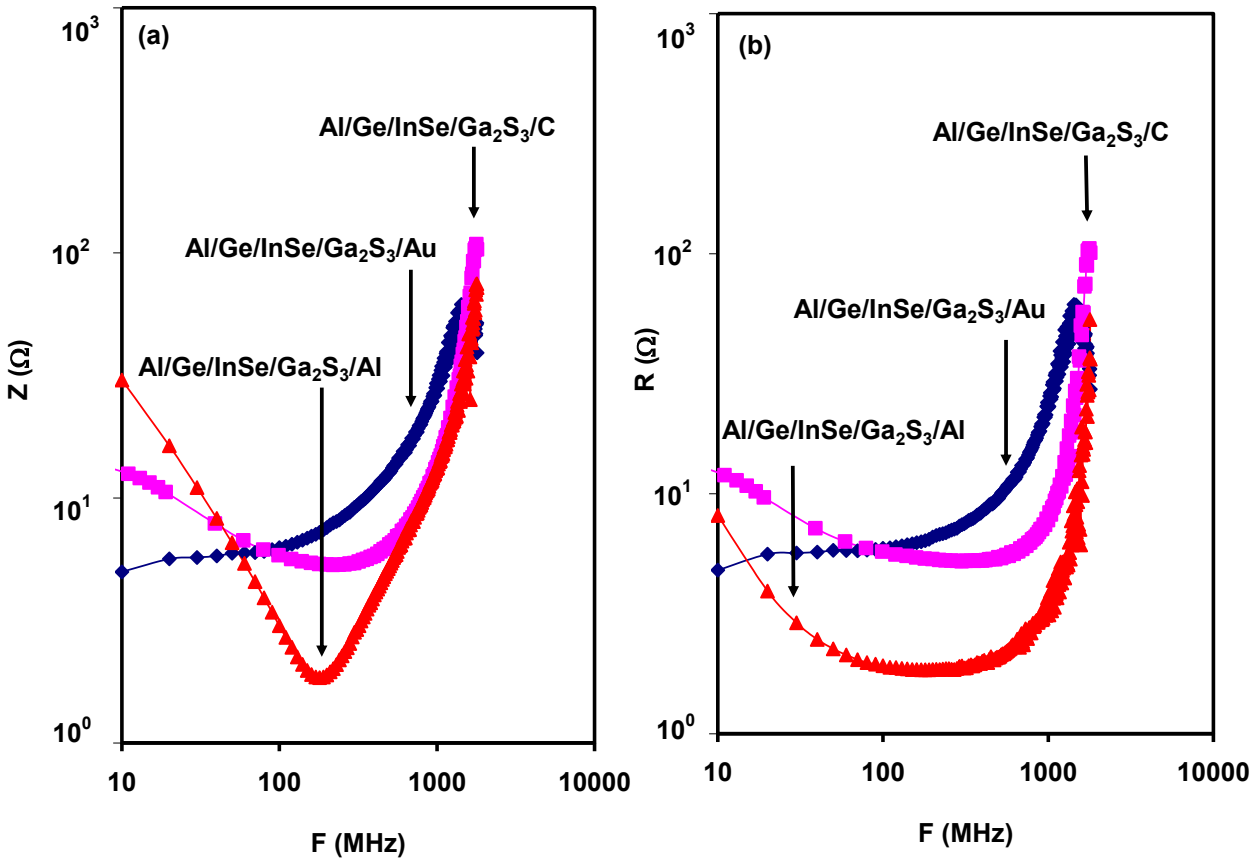

Fig. 4.12 (a) the impedance and (b) the resistance spectra for the device in the frequency range of 1.0 MHz-1.8 GHz.

The data shown in figure 4.13 indicates the increasing of reactance with increasing frequency. It is observed that the Al/pnn/C and Al/pnn/Al spectra starts with negative reactance and then rises. The negative total reactance means the overall circuit is capacitive circuit. The resonance *LC* tank (demonstrated in inset 2(b) of figure 4.11) occurs at zero total reactance, when the inductive reactance of the inductor is equal in value to the capacitive reactance of the capacitance leading to a total reactance of zero. *LC* tanks nominate the device for use as wave oscillators [72]. A differential VCO is also designed for multi-standard RF transceivers [73].

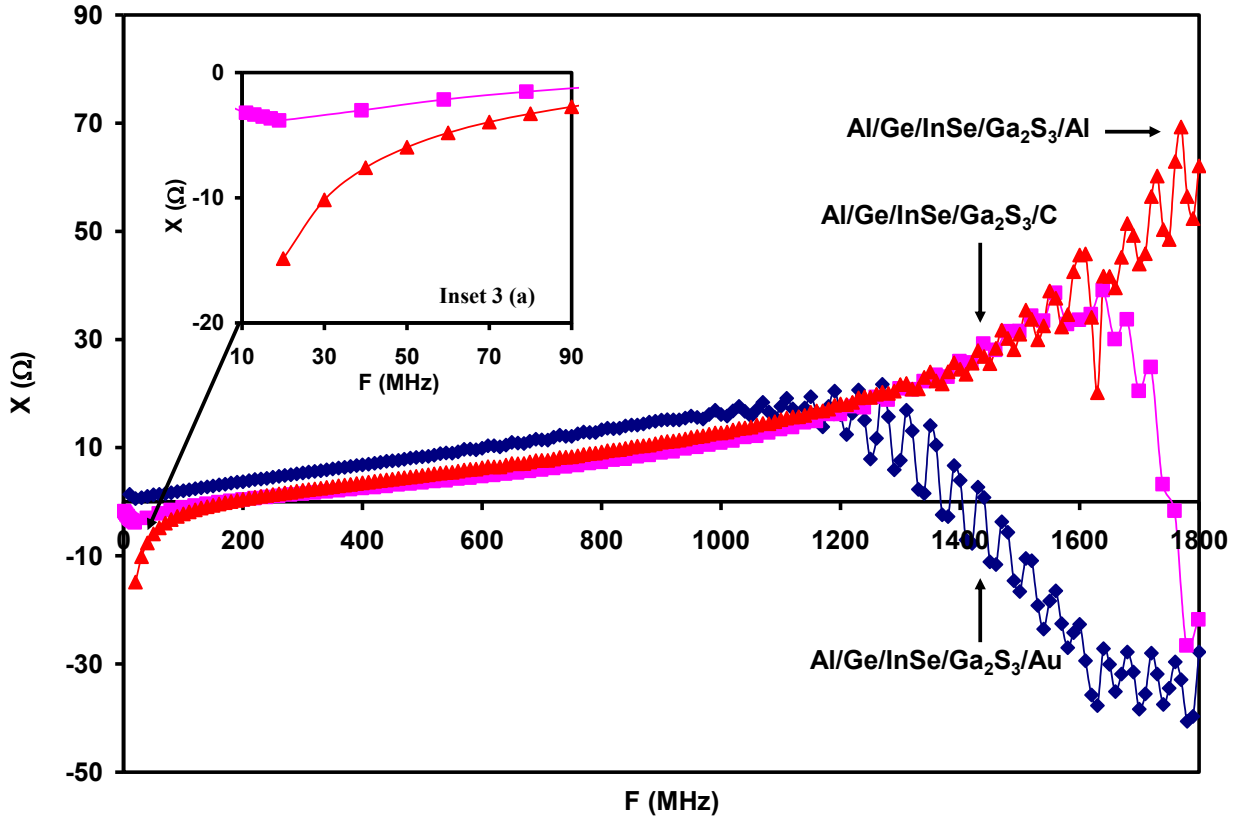

Fig. 4.13: The reactance specta for the pnn device in the frequency range of 1.0 MHz-1.8 GHz.

In addition to the previous consideration, it is possible to explain zero reactance phenomena by considering that the device structure behaves as a parallel circuit (shown in inset 2(b)) consisting of the static (shunt) capacitance C_0 in parallel with the dynamic or motional branch which consists of the series combination of a resistance R_1, an inductance L_1, and a capacitance C_1, which produces a parallel resonance circuit when the resultant current through the parallel combination is in phase with the supplied ac signal voltage. At zero reactance, there is a maximum circulating current between the inductor and the capacitor due to the energy of the oscillations, the motional arm's reactance is zero and the parallel *LC*

circuit acts as an open circuit and the total impedance (Z) value at this point becomes a pure resistance (R) in the circuit. This behavior makes the values of Z and R equal.

The ability of the device to transmit and/or reject ac signals can be concluded from the reflection coefficient, ρ is small for good matches. The reflection coefficient is a complex quantity, has magnitude ρ and angle Θ, and is determined by using equation (2.13).

As it is well readable from fig. 4.14. Direct inverse relation between reflection coefficient and the work function of the metals. The Reflection spectra for the Al/pnn/(C, and Al) behave as low pass filter (LPF) that reject all waves of frequencies less than about 1000 MHz. The ideal wavetrap occurs at about 1400 GHz in the case of Al/pnn/Au and this indicates a good improved filtering properties.

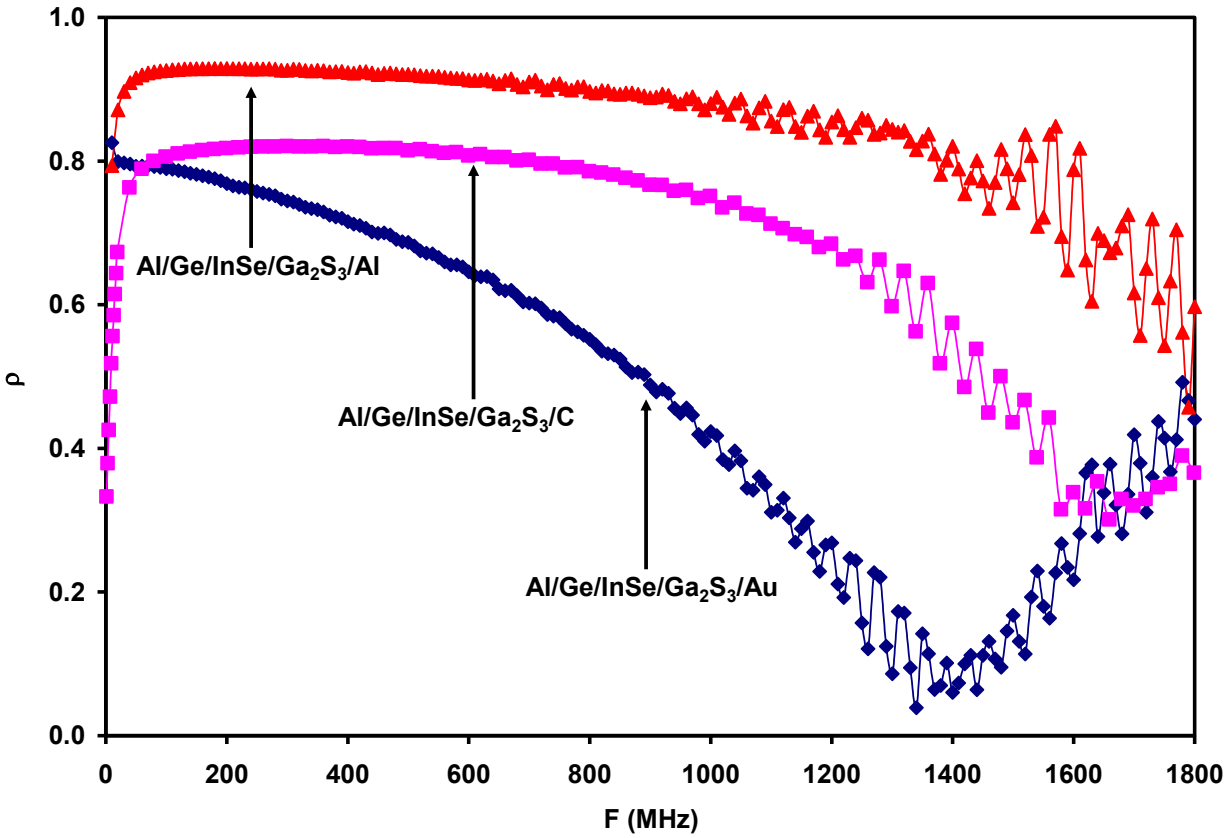

Fig. 4.14: The reflection coefficient for the pnn heterojunction as a function of frequency in the range of 1.0 MHz-1.8 GHz.

One of the most important features of the proposed LPF is acheived when a very good return loss and VSWR are obtained. Very interesting characteristics are observed for the device in figure 4.15 and figure 4.16.

The return loss (equation (2.14)) is a measure of the power which is not absorbed by the device and is returned to the source. For the pnn devices, the reflection coefficient of Al/pnn/Au (figure 4.14) decreases from 0.85 to 0.025 at 1405 MHz, so the return loss is greater than 20 dB (about 32 dB), it reduces from 0.78, and 0.90 for Al/pnn/ (C and Al) to 0.26, and 0.45, respectively. So the return loss is 11.7, and 7.0 dB, respectively.

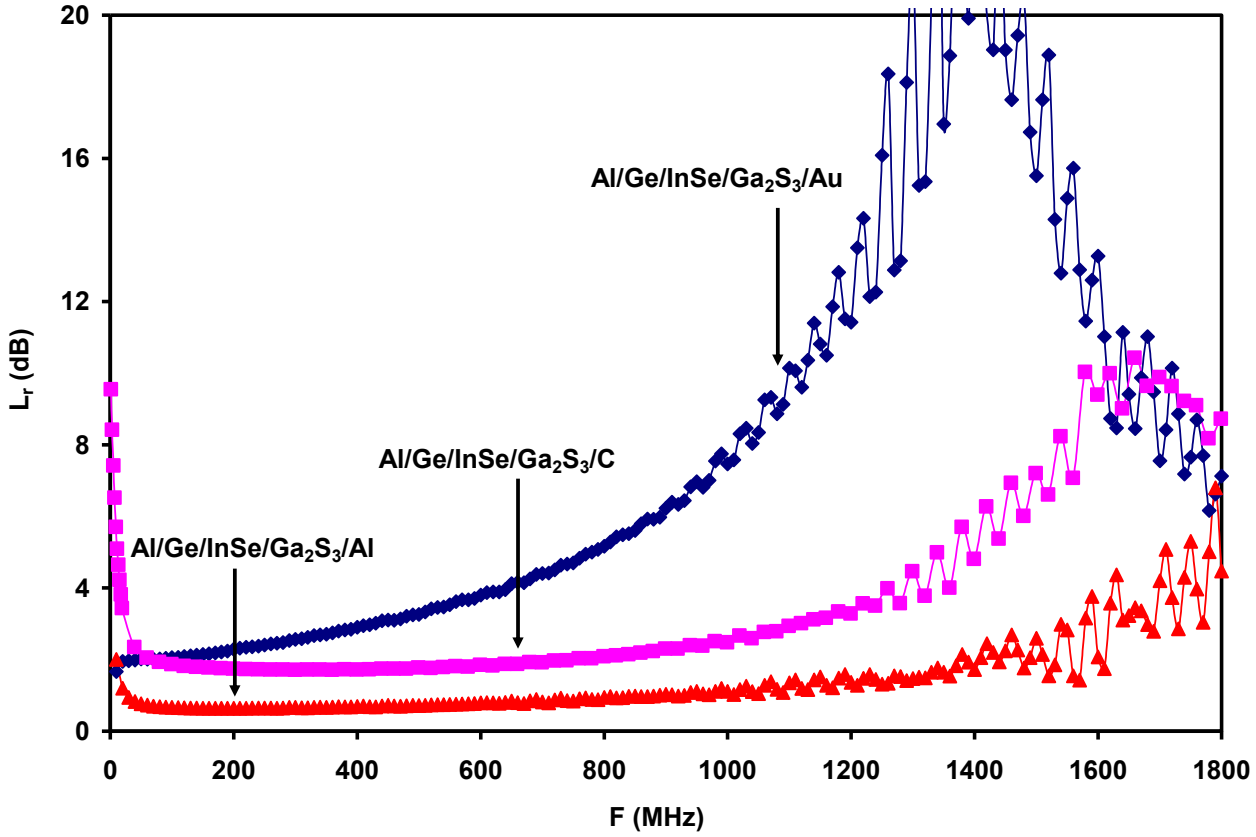

Fig. 4.15: The return loss for the pnn heterojunction as a function of frequency in the range of 1.0 MHz-1.8 GHz.

Figure 4.16 depicts the voltage standing wave ratio (VSWR). Which is defined as the ratio of the maximum voltage to the minimum voltage in a standing wave patterns, it is useful to respect the peak voltage that can be found on a line under non ideal match conditions. It is also a popular measure of the goodness of a match. The VSWR is calculated by using equation (2.12).

The minimum VSWR we get, the better performance we obtain. VSWR of 1 characterized perfect match, while a short or open circuit is producing a VSWR of ∞.

As it is clearly seen from the figure, the shift of VSWR between the devices is due to the work function of metal contact in each pnn device, the lower work function obtained smaller VSWR and better match. The measured VSWR of the pnn/(Au, C and Al) candidates the pnn devices to use in microwave and millimeter-wave ultra-wideband (UWB) applications [74, 75].

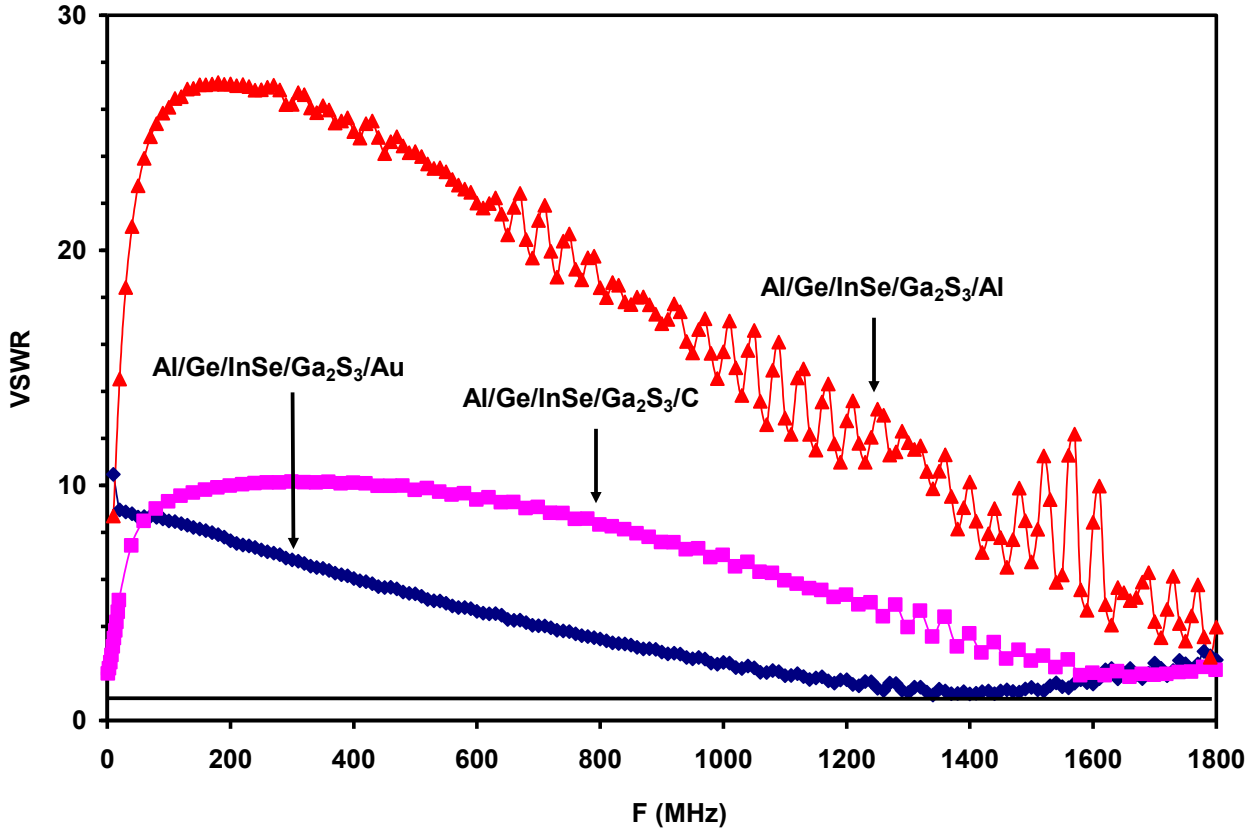

Fig.4.16: The voltage standing wave ratio spectrum with frequency.

4.4 Current- Voltage Characteristics

When the germanium thin film was tested by the hot-probe technique, it displayed p-type conduction. The same technique revealed the n-type nature of conduction for both InSe and Ga_2S_3 films. Thus, the heterojunction (Ge/InSe/Ga_2S_3) represents a pn^+ junction. The main difference between the isotype (p–p) and anisotype (p–n) heterojunction is that the current injection is due to majority and minority carriers in the isotype and anisotype devices respectively. The recorded current (*I*)–voltage (*V*) characteristics of the Al/n-Ga_2S_3 Schottky diode being built on the surface of a n-type InSe layer built on p-type Ge layer grown on vacuum deposited aluminum film are presented in figure 4.17. The data are registered at room temperature in the applied voltage range of 0 to ±1.6 V in 0.01 V steps. The positive terminal of the voltage source is connected to the Al/Ga_2S_3 side. The negative electrode is connected to the Al electrode. The aluminum is used to force the creation of a Schottky barrier at Ga_2S_3 side since the work function of Al (4.23 eV) [2] is larger than the n-type Ga_2S_3 (3.46 eV) [76, 77]. This Schottky barrier is n-type majority carrier device under forward biasing conditions. The Ge side of the device is also contacted to Al metal as it creates another Schottky device with p-type majority carriers, since the work function of Ge is 5.02 eV [78].

As figure 4.17 presents, there is a leakage current at the reverse direction. It is mainly ascribed to more than one reason like the thermal generation of minority carriers by the diffusion across the junction or internal field emission because of the tunneling of carriers through energy barriers as they find thin region during the forward biasing process [79]. In addition to the electron-hole pairs in the depletion region and this may be attributed to the image force

of carriers emitted from metal into the semiconductor [22, 31, 80]. Image force is established when image charges are build up in the metal electrode as the carriers approach the metal–semiconductor interface. The effective barrier height is reduced by the potential associated with these charges.

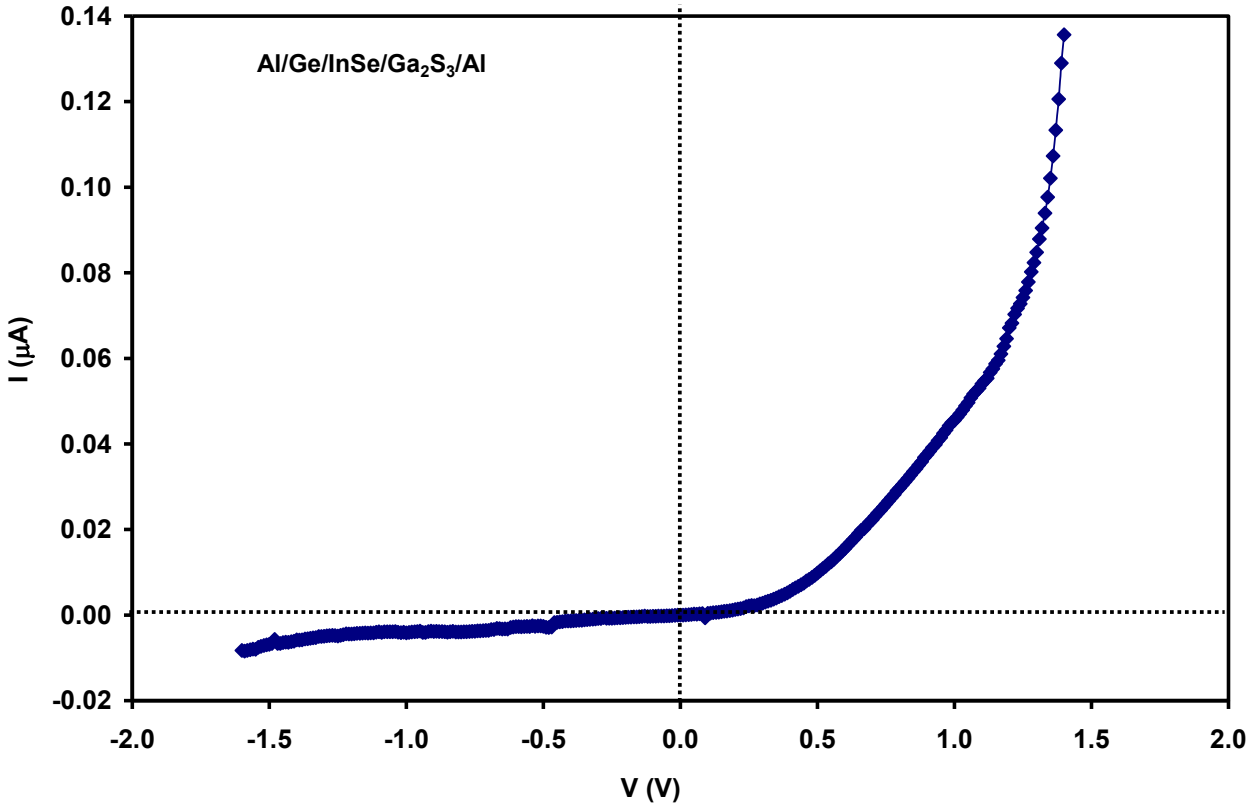

Fig. 4.17: the current voltage characteristics of Al/Ge/InSe/ Ga_2S_3/Al hybrid device.

In order to give significance to the experimental reverse current behavior, the logarithmic current dependence on the square root of the applied voltage illustrates an electric field assisted tunneling current transport mechanism in which the current is governed by the Richardson- Schottky (RS) effects [81]. The charge carriers in the RS mechanism are injected

from the high concentration region (metal electrodes) to low-concentration region (semiconductor) over a potential barrier by electric field- assisted thermionic emission or simply by tunneling [82]. The current–voltage behavior is given by equation (2.15) [29] with A = 7.85 $\times 10^{-3}$ cm^2 is the device area and the barrier height is given by equation (2.16).

As one may easily observe from the figure 4.18. For the reverse biased operation, the dependence of the *ln* (I_R) on $\sqrt{V_R}$ has linearly variation. The slope and intercept of the linear plot presented in figure 4.18, lead to the calculation of the device parameters and indicates the validity of the Richardson-Schottky conduction over the studied range of voltage.

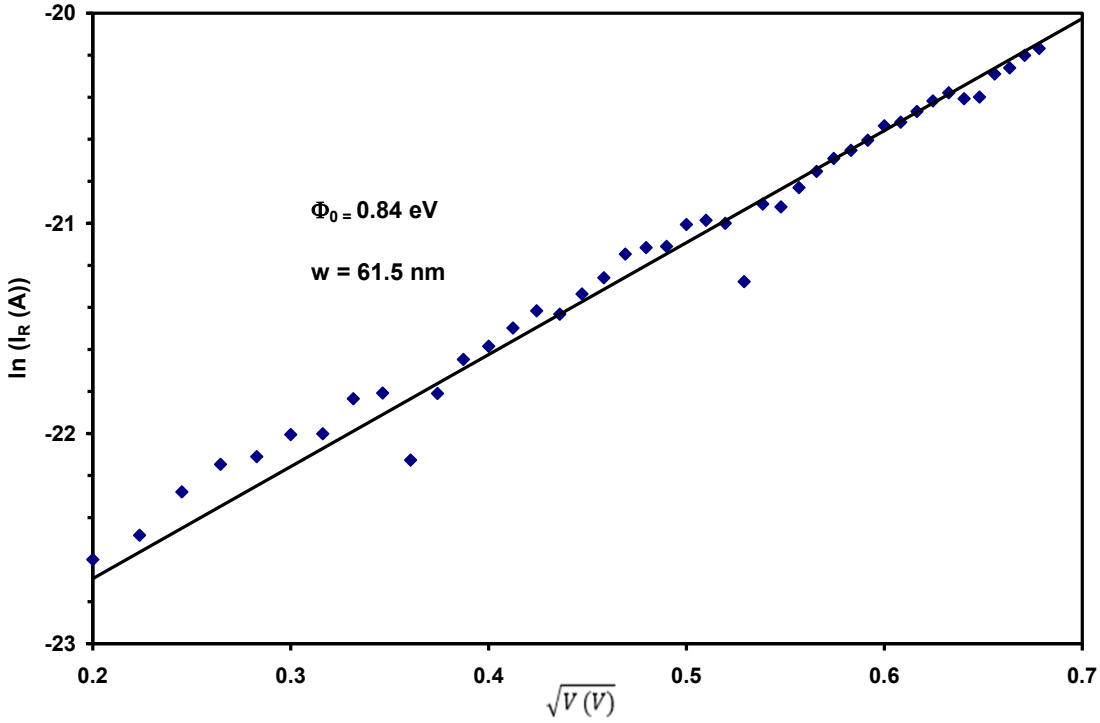

Fig. 4.18: The variation of ln (I) with $\sqrt{V}$ for the reverse bias.

The Richardson constant in equation (2.15) $A^{**} = 120m^*$ is determined as 9.3 $A.cm^{-2}K^{-2}$ assuming an effective mass $m^* = 0.077m_o$ for the Ge/InSe/Ga_2S_3 device. Substituting the

temperature (T) as 300 K and using the intercept of the solid line which is plotted in figure 4.18, the Richardson–Schottky zero electric field energy barrier height (ϕ_0) to the charge flow is revealed as 0.84 eV. In addition, the slope of the same solid line allowed the calculation of the effective barrier width as $w = 0.756 \times 10^{-5}$ cm/ε_r. The real part of the dielectric constant for the three layers was determined optically from the reflectivity measurements in the range of 300-1100 nm. The width of the interface region w is turns out to be 61.5 nm. This value of the depletion region width is narrow enough and can be regarded as an important reason for preferring the tunneling mechanism for conduction.

On the other hand, in the applied forward biasing range, the I–V analysis was handled assuming a thermionic emission of charge carriers over the barrier height, the ideality factor (η) and the device barrier height (ϕ_b) was evaluated from the chart of $ln\ (I) - V$ as shown in figure 4.19(a). The calculations revealed an ideality factor and barrier height of 6.6 and 0.78 eV, respectively. The value of η being 6.6 is much greater than unity. The deviation is generally ascribed to several reasons such as the bias dependence of the barrier height, additional thermally assisted carrier tunneling [83], electron– hole pair recombination through the depletion region [79], the induced defects, Schottky barrier in-homogeneities, image force lowering effects [31, 84] and device internal series resistance effect that cause particular voltage drop, the less the R_S value is, the lower V_S and the higher the injection current [79]. When the effect of IR_S is less dominant, in high current injection region where Rs remains constant, the diode reflects typical Schottky barrier characteristics.

Following the same method described in reference [31] that examines the device series resistance effects on the device ideality factor and barrier height and using the equations which follows. The derivatives of $dV_F/d\ (\ln(I_F))$ had been evaluated and plotted as a function

of I_F in figure 4.19(b). The slope and the intercept of the straight solid line indicated an ideality factor and series resistance of ~3.79 and 9.76 MΩ, respectively. Consistently, the Cheung method [31], which is also based on thermionic emission theory and presented by the following equations to detect the series resistance effect through redefining the device current as [31].

$$I = AA^{*}T^{2}exp\left(\frac{-q\phi_b}{kT}\right)\left(exp\left(\frac{q(V-IR_s)}{nkT}\right)-1\right) \tag{4.5}$$

By evaluating the derivative of $\frac{dV}{d(lnI)}$, one may obtain,

$$\frac{dV}{d(lnI)} = IR_s + n\left(\frac{kT}{q}\right) \tag{4.6}$$

Leading to Cheung function [31, 85].

$$H(I) = V - n\left(\frac{kT}{q}\right)ln\left(\frac{1}{AA^{**}T^{2}}\right) = IR_s + n\phi_b \tag{4.7}$$

Thus, in accordance with previous equation, the linear dependence of $\frac{dV}{d(lnI)}$ on I displayed in figure 4.19(b). The slope and intercept of the solid line allowed computation of the series resistance and ideality factor as 9.76 MΩ and 3.79, respectively. The values are imposed in equation (H) to determine H (I) which is shown in figure 4.19(c). Even though the ideality factor decreases from 6.6 to 3.79 by series resistance effect elimination, it still greater than unity.

Here, the factor *IRs* represents the voltage drop across the series resistance of the Schottky diode. *H* (*I*) was evaluated and plotted as a function of *I* in figure 4.19(c). The plot should

give a straight line, its slope and will give a second determination of R_s as 9.80 MΩ. By having two values of R_s, this case is checking the consistency of Cheung's approach. The values of R_s obtained from figures 4.19(b) and 4.19(c) which are 9.76 MΩ and 9.80 MΩ respectively are in good agreement with each other. The average value of the series resistance is 9.78 MΩ. The y-axis intercept of the solid line shown in the figure 4.19(c) allowed determining the forward bias barrier height as 0.81 eV, which is also closed to the 0.78 eV value that was obtained without excluding the series resistance effect.

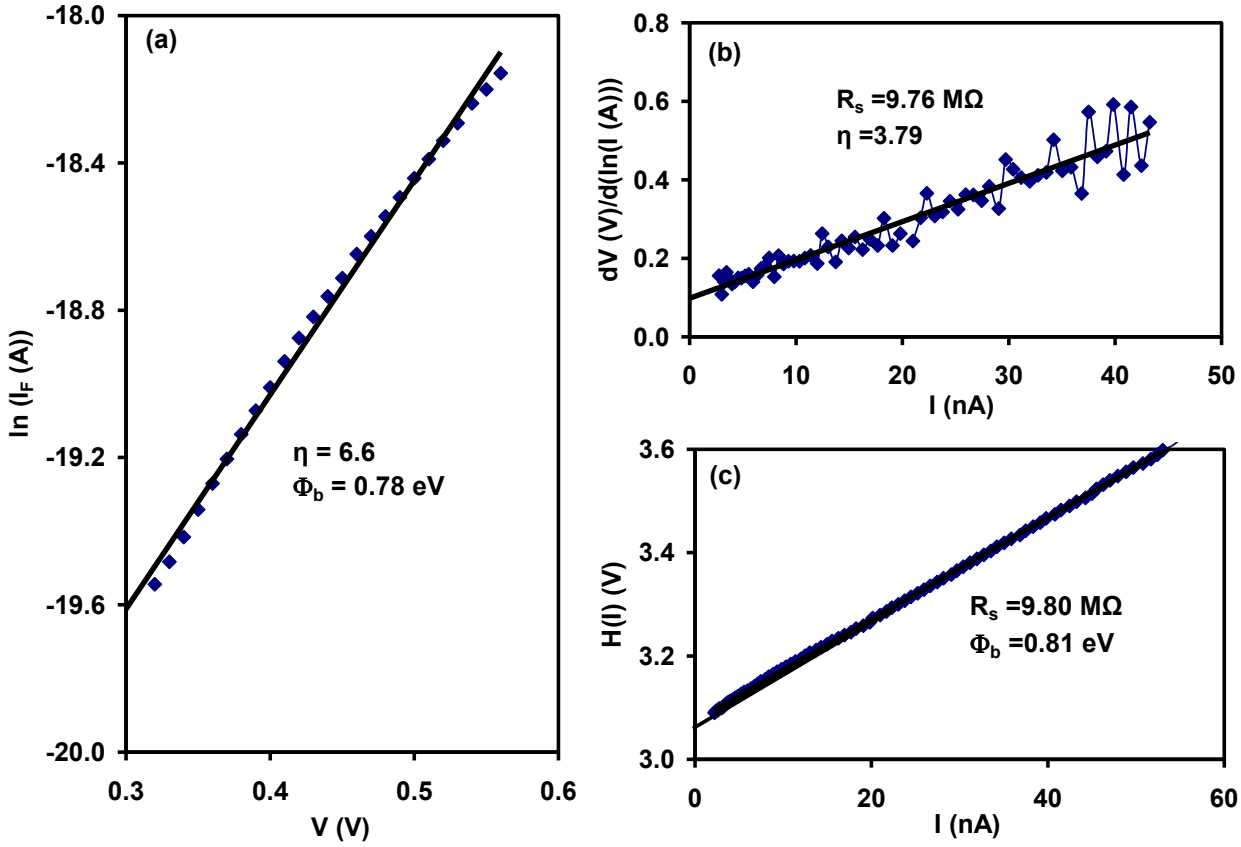

Fig. 4.19: (a) Plots of ln (I) versus V, (b) dV/d(ln I) versus I, and (c) H(I) versus I for the pnn hybrid at forward biasing.

4.5 Band Diagram Construction

The energy band diagram for Al/Ge/InSe/Ga_2S_3/Al hybrid device is designed with the help of optical and electrical data and displayed in the figure 4.20. As can be seen from the energy band diagram the pn^+ device is modeled as two Schottky diodes; one is forward biased and the other is reversed biased. The electron affinity of Ge is 4.13 eV [31]. Since the work function of aluminum is 4.23 eV [2], and the indirect energy band gap of the Ge substrate is 0.80 eV (determined from the absorption coefficient), the Ge work function is 5.02 eV, then the Schottky barrier height $\phi_{Al/Ge} = q\chi_{Ge} + E_{g_{Ge}} - q\phi_{Al}$ is 0.70 eV and the built-in voltage of the Al/Ge interface, $V_{bi} = \chi_{Ge} + E_{g_{Ge}} - (E_F - E_V) - \phi_{Al}$ is supposed to exhibit a value of 0.2 V. The barrier height at the Al/ Ga_2S_3 interface is $\phi_{Bn} = q\phi_{Al} - q\phi_{Ga_2S_3}$= 0.93 eV. $V_{bi} = \phi_{Al} - \phi_{Ga_2S_3}$ = 0.77 V.

The most reported energy band gaps for the n-type In_2Se_3 and n-type Ga_2S_3 are 1.80, 3.15 eV, the electron affinities are 4.55 eV [51], 3.30 eV [86], the work functions are 4.69, 3.45 eV, respectively. The conduction band discontinuity $\Delta E_{C_1} = q\chi_{Ge} - q\chi_{InSe}$, is 0.42 eV. $\Delta E_{C_2} = q\chi_{InSe} - q\chi_{Ga_2S_3}$ is 1.25 eV and the valence band discontinuity can be calculated from the relation $\Delta E_{V_1} = E_{g_{Ge}} - E_{g_{InSe}} - \Delta E_{C_1}$ being found to be 0.58 eV. $\Delta E_{V_2} = E_{g_{InSe}} - E_{g_{Ga_2S_3}} - \Delta E_{C_2}$ is 0.10 eV.

In the light of the constructed energy band diagram, the working principle of the heterojunction device can be described as follows;

When the negative current is applied from the Al/Ge Schottky side (majority carriers device), it is reversed biased, the p-n junction is reverse biased and the electrons in the InSe layer are pulled away from the depletion region at the Ge/InSe interface. The holes, as a result, in Ge

layer will be pulled toward the Al metal, therefore, the depletion region widens. As a result, the electrons in the Ga_2S_3 will also be pulled away the n^+ junction. Because electrons of InSe become closer to InSe/ Ga_2S_3 interface (n^+ type) at that interface the depletion width also widens, this behavior causes an increase in the device series resistance, blocking the current through the diode (few μA).

When a diode is connected in a reverse Bias condition, a negative voltage is applied to the p-type material that attracts the holes away from the junction towards the negative electrode and a positive voltage is applied to the n-type material which attracts electrons towards the positive electrode and away from the junction. At Forward Bias condition, a positive voltage is applied to the p-type material and a negative voltage is provided to the n-type material and, if this external voltage becomes greater than the value of the potential barrier, approx. 0.3 volts for Ge, the potential barriers opposition will be overcome and current becomes to flow.

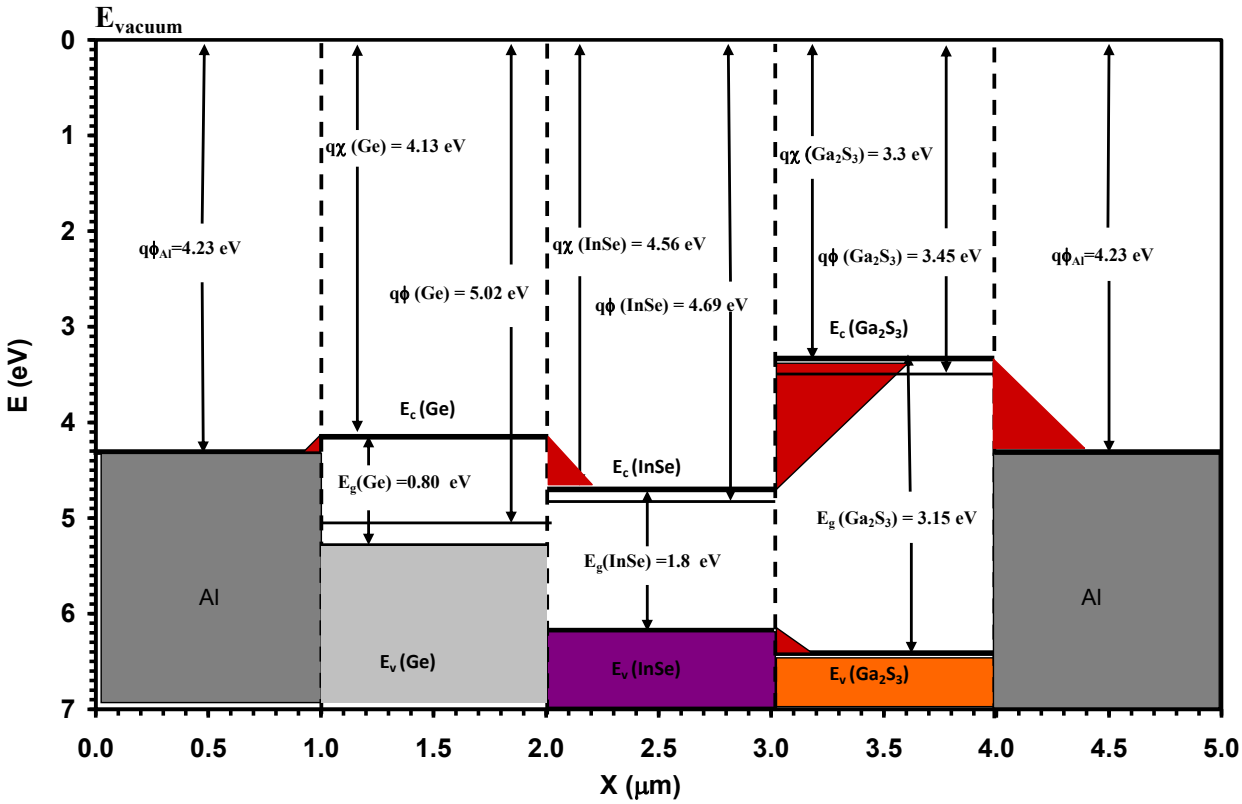

Fig. 4.20: The band diagram of the Al/Ge/InSe/Ga_2S_3/Al hybrid.

Chapter Five
Conclusions

In this work, a 400 nm thick InSe/Ga_2S_3 interface was fabricated on 200 nm thick germanium substrate using the vacuum deposition technique. The structural analysis which were carried out by different techniques have shown the physical nature of the films in which correct stoichiometry presented by Ga_2S_3 and InSe chemical formulas appeared from the compositional analysis. In addition, the diamond structured Ge films allowed the growth of the hexagonal unit cells of InSe on its surface. Even though the structures of Ge and InSe are different and the Ga_2S_3 grow in amorphous phase onto glass substrates of temperatures of 300 K, when grown onto InSe surface they exhibited monoclinic shaped unit cells which refer to $\alpha -$ phase of Ga_2S_3. When these heterojunction devices were subjected to optical tests through the measurements of transmittance and absorbance a remarkable change in the energy band gaps that lead to a valence band offsets of ~ 1.35 eV was achieved at the interface between Ge and InSe. The value is large enough to produce thin film transistors as it allow quantum confinement of valence electrons and holes leading to larger absorbance values.

On the other hand, when the optical data were employed to estimate the dielectric spectra of the hybrid device an interesting information was achieved. Particularly, the dielectric spectra modeling via Drude-Lorentz approach, revealed electron plasmon coupling with frequencies at gigahertz levels. The scattering time of electron oscillates at femtosecond levels leading to an improvement of the drift mobility of the electrons in the hybrid device. It is also seen that the Ge/InSe/Ga_2S_3 thin film devices are suitable for ac signal propagation. This observation was verified with the impedance spectroscopy which show the possibility of using these thin

film transistors for wave trapping and for application where parasitic cancelation of capacitance is necessary. The device actualize this cancellation through the negative capacitance character which exhibit in its natural performance. In addition, the current-voltage characteristics on the device through the Al electrodes which forces back to back Schottky structure allowed the investigation of the current conduction mechanism in the device. The thermionic emission of charged particles of the Schottky barrier height was observed to be the dominant mechanism. The calculated Schottky-Richardson parameters with the band offsets obtained from the optical analysis allowed the sketching of the energy band diagram of the hybrid device. In accordance with the energy band diagram and the observed optical, dielectric and electrical performance of the device with the resonance and antiresonance phenomena it can be concluded that with its thin structure and compact size, the Ge/InSe/Ga_2S_3 hybrid structure is a promising device that can be used in optoelectronics as well as microwave trapping, parasitic capacitance conciliator and memory clocks.

References

[1] Nadimpalli, Siva PV, Rajasekhar Tripuraneni, and Vijay A. Sethuraman. "Real-time stress measurements in germanium thin film electrodes during electrochemical lithiation/delithiation cycling." *Journal of The Electrochemical Society* 162.14 (2015): A2840-A2846.

[2] Al Garni, S. E., and A. F. Qasrawi. "Design and characterization of (Al, C)/p-Ge/p-BN/C isotype resonant electronic devices." *physica status solidi (a)* 212.8 (2015): 1845-1850.

[3] Al Garni, S. E., and A. F. Qasrawi. "Optical analysis of Ge/MgO and Ge/BN thin layers designed for terahertz applications." *Materials Science in Semiconductor Processing* 31 (2015): 678-683.

[4] Mohan, A., J. Suthagar, and T. Mahalingam. *Investigation on the Structural and Optical Properties of Thermally Evaporated Indium Selenide Compound Material for Solar Cell Application*. Diss. Sumy State University, 2013.

[5] Tamalampudi, Srinivasa Reddy, et al. "High performance and bendable few-layered InSe photodetectors with broad spectral response." *Nano letters* 14.5 (2014): 2800-2806.

[6] Feng, Wei, et al. "Performance improvement of multilayer InSe transistors with optimized metal contacts." *Physical Chemistry Chemical Physics* 17.5 (2015): 3653-3658.

[7] Yılmaz, K., M. Parlak, and Ç. Erçelebi. "Investigation of photovoltaic properties of amorphous InSe thin film based Schottky devices." *Semiconductor Science and Technology* 22.12 (2007): 1268.

[8] Qasrawi, Atef F., and Hazem K. Khanfar. "Design and Applications of Al/InSe/BN/Ag Hybrid Device." *IEEE Sensors Journal* 15.6 (2015): 3603-3607.

[9] Huang, Zhiming, et al. "Ga 2 S 3: Optical properties and perspectives for THz applications." *Infrared, Millimeter, and Terahertz waves (IRMMW-THz), 2015 40th International Conference on*. IEEE, 2015.

[10] Othonos, Katerina M., et al. "Ultrafast Spectroscopy and Red Emission from β-Ga 2 O 3/β-Ga 2 S 3 Nanowires." *Nanoscale research letters* 10.1 (2015): 304.

[11] Ahamad, Tansir, and Saad M. Alshehri. "Green Synthesis and Characterization of Gallium (III) Sulphide (α-Ga2S3) Nanoparicles at Room Temperature." *Nano Hybrids*. Vol. 6. Trans Tech Publications, 2014.

[12] Liu, H. F., et al. "Synthesis and phase evolutions in layered structure of Ga2S3 semiconductor thin films on epiready GaAs (111) substrates." *ACS applied materials & interfaces* 6.5 (2014): 3501-3507.

[13] Alharbi, S. R., and A. F. Qasrawi. "Dielectric Dispersion in Ga2S3 Thin Films." *Plasmonics* (2016): 1-5.

[14] Li, Shasha, et al. "Monophase γ-In 2 Se 3 thin film deposited by magnetron radio-frequency sputtering." *Vacuum* 99 (2014): 228-232.

[15] Biswal, Laxmidhar, S. K. Som, and Suman Chakraborty. "Thin film evaporation in microchannels with slope-and curvature-dependent disjoining pressure." *International Journal of Heat and Mass Transfer* 57.1 (2013): 402-410.

[16] Kumar, Challa SSR, ed. *X-ray and Neutron Techniques for Nanomaterials Characterization*. Springer Berlin Heidelberg, 2015.

[17] Bhargava, A. K., and C. P. Sharma. *Mechanical Behaviour and testing of materials*. PHI Learning Pvt. Ltd., 2011.

[18] Kuttge, M., et al. "Analysis of the propagation of terahertz surface plasmon polaritons on semiconductor groove gratings." *Journal of applied physics* 101.2 (2007): 023707.

[19] West, Paul R., et al. "Searching for better plasmonic materials." *Laser & Photonics Reviews* 4.6 (2010): 795-808.

[20] Pannipitiya, Asanka, et al. "Improved transmission model for metal-dielectric-metal plasmonic waveguides with stub structure." *Optics express* 18.6 (2010): 6191-6204.

[21] Pankove, Jacques I. *Optical processes in semiconductors*. Courier Corporation, 2012.

[22] Solar Energy for Fuels edited by Harun Tüysüz, Candace K. Chan

[23] Practical Electrical Engineering - Page 9-31 Sergey N. Makarov, Reinhold Ludwig, Stephen J. Bitar – 2016

[24] Al Garni, Sabah E., and Atef F. Qasrawi. "Impedance Spectroscopic Analysis of the InSe/ZnSe/InSe Interface." *IEEE Transactions on Electron Devices* 64.1 (2017): 244-249.

[25] Darimireddy, Naresh Kumar, R. Ramana Reddy, and A. Mallikarjuna Prasad. "Design of triple-layer double U-slot patch antenna for wireless applications." *Journal of applied research and technology* 13.5 (2015): 526-534.

[26] Bowick, Christopher. RF circuit design. Newnes, 2011.

[27] Lüth, Hans. *Surfaces and interfaces of solid materials*. Springer Science & Business Media, 2013.

[28] Simon, Jacques, and J-J. Andre. *Molecular semiconductors: photoelectrical properties and solar cells*. Springer Science & Business Media, 2012.

[29] Jafar, MM Abdul-Gader. "High-bias current–voltage–temperature characteristics of undoped rf magnetron sputter deposited boron carbide (B5C)/p-type crystalline silicon - heterojunctions." *Semiconductor science and technology* 18.1 (2002): 7.

[30] Khanfar, Hazem K. "Fabrication and characterization of Ag/BN/Ni microwave rejection-band filters." *IEEE Transactions on Electron Devices* 61.6 (2014): 2154-2157.

[31] Sze, Simon M., and Kwok K. Ng. *Physics of semiconductor devices*. John wiley & sons, 2006.

[32] Lu, Chao, and Alvin Warren Czanderna, eds. *Applications of piezoelectric quartz crystal microbalances*. Vol. 7. Elsevier, 2012.

[33] Mattox, Donald M. *Handbook of physical vapor deposition (PVD) processing*. William Andrew, 2010.

[34] Reimer, Ludwig. "Scanning electron microscopy: physics of image formation and microanalysis." (2000): 1826.

[35] Simon, R. A., et al. "Disorder induced interface states and their influence on the Al/Ge nanowires Schottky devices." *Journal of Applied Physics* 114.24 (2013): 243705.

[36] Morgunov, R. B., et al. "Electron spin resonance of charge carriers and antiferromagnetic clusters in Ge 0.99 Cr 0.01 nanowires." *Journal of Applied Physics* 105.9 (2009): 093922.

[37] O. Madelung, *Semiconductors: data handbook*. (Springer Science & Business Media, New York, (2012)).

[38] Meng, Xiangbo, et al. "Gallium Sulfide–Single-Walled Carbon Nanotube Composites: High-Performance Anodes for Lithium-Ion Batteries." *Advanced Functional Materials* 24.34 (2014): 5435-5442.

[39] Lim, Young Rok, et al. "Composition-tuned Sn x Ge 1− x S nanocrystals for enhanced-performance lithium ion batteries." *RSC Advances* 4.104 (2014): 60058-60063.

[40] Ulaganathan, Rajesh Kumar, et al. "High photosensitivity and broad spectral response of multi-layered germanium sulfide transistors." *Nanoscale* 8.4 (2016): 2284-2292.

[41] Koch, Carl, et al. *Structural nanocrystalline materials: fundamentals and applications*. Cambridge University Press, 2007.

[42] Sério, S., et al. "Influence of O 2 partial pressure on the growth of nanostructured anatase phase TiO 2 thin films prepared by DC reactive magnetron sputtering." *Materials Chemistry and Physics* 126.1 (2011): 73-81.

[43] Axelevitch, A., B. Gorenstein, and G. Golan. "Investigation of optical transmission in thin metal films." *Physics Procedia* 32 (2012): 1-13.

[44] Bornoz, Pauline, et al. "A bismuth vanadate–cuprous oxide tandem cell for overall solar water splitting." *The Journal of Physical Chemistry C* 118.30 (2014): 16959-16966.

[45] Qasrawi, Atef F., and N. M. Gasanly. "Energy Band Diagram and Current Transport Mechanism In p-MgO/n-Ga 4 Se 3 S." *IEEE Transactions on Electron Devices* 62.1 (2015): 102-106.

[46] Park, Sung Heum, et al. "Bulk heterojunction solar cells with internal quantum efficiency approaching 100&percnt." *Nature photonics* 3.5 (2009): 297-302.

[47] Alharbi, S. R., and A. F. Qasrawi. "Optical and electrical performance of Yb/InSe interface." *Materials Science in Semiconductor Processing* 43 (2016): 60-64.

[48] Park, Won Il, et al. "Hybrid semiconductor nanostructures with graphene layers." *Semiconductor Nanostructures for Optoelectronic Devices*. Springer Berlin Heidelberg, 2012. 167-195.

[49] Uchida, Yasutaka, et al. "Properties of electrodeposited germanium thin films." *physica status solidi (c)* 11.11-12 (2014): 1661-1664.

[50] Ho, Ching-Hwa, and Yun-Ju Chu. "Bending Photoluminescence and Surface Photovoltaic Effect on Multilayer InSe 2D Microplate Crystals." *Advanced Optical Materials* 3.12 (2015): 1750-1758.

[51] Chuang, Ching-An, et al. "The study of flexible emission and photoconductivity in 2D layered InSe toward an applicable 1000-nm light emitter and absorber." *Applied Physics A* 123.3 (2017): 197.

[52] Ichimura, Masaya, and Shoichi Kawai. "Band alignment at the CdS/FeS2 interface based on the first-principles calculation." *Japanese Journal of Applied Physics* 54.3 (2015): 038002.

[53] Jia, C. H., et al. "Valence band offset of ZnO/BaTiO3 heterojunction measured by X-ray photoelectron spectroscopy." *Applied Physics A* 99.2 (2010): 511-514.

[54] Kayed, T. S., A. F. Qasrawi, and Khaled A. Elsayed. "Band offsets and optical conduction in the CdSe/GaSe interface." *Current Applied Physics*16.7 (2016): 772-776.

[55] Mourad, Daniel, et al. "Determination of valence-band offset at cubic CdSe/ZnTe type-II heterojunctions: A combined experimental and theoretical approach." *Physical Review B* 86.19 (2012): 195308.

[56] Antanovich, A. V., et al. "Colloidal synthesis and optical properties of type-II CdSe–CdTe and inverted CdTe–CdSe core–wing heteronanoplatelets." *Nanoscale* 7.17 (2015): 8084-8092.

[57] Devi, Vanita, et al. "Band offset studies in pulse laser deposited Zn1− xCdxO/ZnO hetero-junctions." *Journal of Applied Physics* 117.22 (2015): 225305.

[58] Long, Wei, Yang Li, and Raymond T. Tung. "Schottky barrier height systematics studied by partisan interlayer." *Thin Solid Films* 557 (2014): 254-257.

[59] L. Zhu, J.K.Luo, Shao, W.I.Milne, S.o.l. Ener, Mater. Sol. Cells 111 (2013)141–145.

[60] Qasrawi, A. F., S. E. Al Garni, and N. M. Gasanly. "Characterization of the MgO/GaSe 0.5 S 0.5 heterojunction designed for visible light communications." *Materials Science in Semiconductor* Processing 39 (2015): 377-383.

[61] Kayed, T. S., A. F. Qasrawi, and Khaled A. Elsayed. "Optical characterization of the MgO/InSe interface." *physica status solidi (b)* 252.3 (2015): 621-625.

[62] Qasrawi, A. F. "Fabrication of Al/MgO/C and C/MgO/InSe/C tunneling barriers for tunable negative resistance and negative capacitance applications." *Materials Science and Engineering: B* 178.12 (2013): 851-856.

[63] Qasrawi, A. F., Hazem K. Khanfar, and Renal RN Kmail. "Optical conduction in amorphous GaSe thin films." *Optik-International Journal for Light and Electron Optics* 127.13 (2016): 5193-5195.

[64] Eldlio, Mohamed, Franklin Che, and Michael Cada. "Drude-Lorentz Model of Semiconductor Optical Plasmons." *IAENG Transactions on Engineering Technologies*. Springer Netherlands, 2014. 41-49.

[65] Irisawa, T., et al. "Hole density dependence of effective mass, mobility and transport time in strained Ge channel modulation-doped heterostructures." *Applied physics letters* 82.9 (2003): 1425-1427.

[66] Feng, Wei, et al. "Back gated multilayer InSe transistors with enhanced carrier mobilities via the suppression of carrier scattering from a dielectric interface." *Advanced Materials* 26.38 (2014): 6587-6593.

[67] Wu, Qiyang, et al. "Frequency tuning range extension in LC-VCOs using negative-capacitance circuits." *IEEE Transactions on Circuits and Systems II: Express Briefs* 60.4 (2013): 182-186.

[68] Çetinkaya, H. G., et al. "Investigation of negative dielectric constant in Au/1% graphene (GP) doped-Ca1. 9Pr0. 1Co4Ox/n-Si structures at forward biases using impedance

spectroscopy analysis." *Journal of Materials Science: Materials in Electronics* 26.5 (2015): 3186-3195.

[69] Kmail, Renal RN, and A. F. Qasrawi. "Physical design and dynamical analysis of resonant–antiresonant Ag/MgO/GaSe/Al optoelectronic microwave devices." *Journal of Electronic Materials* 44.11 (2015): 4191-4198.

[70] Qasrawi, A. F., and N. M. Gasanly. "Investigation of the electrical parameters of Ag/p-TlGaSeS/C Schottky contacts." *Materials Science and Engineering: B* 177.12 (2012): 981-985.

[71] Qasrawi, Atef F., Hazem K. Khanfar, and N. M. Gasanly. "MgO/GaSe 0.5 S 0.5 Heterojunction as Photodiodes and Microwave Resonators." *IEEE Sensors Journal* 16.3 (2016): 670-674.

[72] Li, Lianming, Patrick Reynaert, and Michiel SJ Steyaert. "Design and analysis of a 90 nm mm-wave oscillator using inductive-division LC tank." *IEEE Journal of Solid-State Circuits* 44.7 (2009): 1950-1958.

[73] Jain, Sanjeev, Sheng-Lyang Jang, and Nikolay T. Tchamov. "Tuned LC-Resonator Dual-Band VCO." *IEEE Microwave and Wireless Components Letters* 26.3 (2016): 204-206.

[74] Dastranj, Aliakbar, and Bijan Abbasi-Arand. "High-Performance 45° Slant-Polarized Omnidirectional Antenna for 2–66-GHz UWB Applications." *IEEE Transactions on Antennas and Propagation* 64.2 (2016): 815-820.

[75] Naser-Moghadasi, Mohammad, et al. "Low SAR PIFA Antenna for Wideband Applications." *IETE Journal of Research* 62.5 (2016): 564-570.

[76] work function of ga2s3

[77] Sharma, B. L., ed. *Metal-semiconductor Schottky barrier junctions and their applications*. Springer Science & Business Media, 2013.

[78] Janardhanam, V., et al. "Depinning of the Fermi level at the Ge Schottky interface through Se treatment." *Scripta Materialia* 69.11 (2013): 809-811.

[79] Tyagi, Man S. *Introduction to semiconductor materials and devices*. John Wiley & Sons, 2008.

[80] Qasrawi, A. F., et al. "Design and characterization of TlInSe 2 varactor devices." *Physica B: Condensed Matter* 406.14 (2011): 2740-2744.

[81] Brune, Dag, et al., eds. *Surface characterization*. John Wiley & Sons, 2008.

[82] Wang, Hailing, et al. "Enhanced electrical properties in ferroelectric thin films on conductive Au–LaNiO 3 nanocomposite electrodes via modulation of Schottky potential barrier." *RSC Advances* 5.126 (2015): 104203-104209.

[83] Yim, Chanyoung, Niall McEvoy, and Georg S. Duesberg. "Characterization of graphene-silicon Schottky barrier diodes using impedance spectroscopy." *Applied Physics Letters* 103.19 (2013): 193106.

[84] Qasrawi, A. F., Shadia Elayyat, and N. M. Gasanly. "Dynamical and passive characteristics of the Ag/TlGaSeS/Ag RF resonators." *Crystal Research and Technology* 47.6 (2012): 615-619.

[85] Rao, L. Dasaradha, et al. "Effect of thermal annealing on the electrical and structural properties of Au/Y/p-type InP Schottky structure." *Vacuum* 119 (2015): 276-283.

[86] Mei-Ling, KONG De-Nian FENG, and YE Dong HUANG Xiao-Ying. "Syntheses, Crystal Structures and Thermal and Optical Properties of Two Organic Templated Gallium Antimony Sulfides." *Chinese Journal of Structural Chemistry* 6 (2010): 015.

List of publications

1. Omareya, Olfat A., A. F. Qasrawi, and S. E. Al Garni. "Effect of Au nanosandwiching on the structural, optical and dielectric properties of the as grown and annealed InSe thin films." *Physica B: Condensed Matter* (2017).

2. Al Garni, S. E., Olfat A. Omariya, and A. F. Qasrawi. "Growth and Characterization of InSe/Ge/InSe interfaces." *Optik-International Journal for Light and Electron Optics* (2017).

Conferences

- Olfat A. Omareya, A.F. Qasrawi, Light Polarization Effects on the Optical Properties of Selenium (poster). Second Palestinian International Conference on Material Science and Nanotechnology. An-Najah National University-Nablus. 2016.

- Olfat A. Omareya, A. F. Qasrawi. Energy Band Diagram and Characterization of InSe/GaS Heterojunction (oral presentation). Fifth Palestinian Conference on Modern Trends in Mathematics and Physics. Arab American University-Jenin. 2016.

- Olfat A. Omareya, A. F. Qasrawi. Design and characterization of Ge based pnn interfaces (oral presentation). Second Palestinian International Graduate Conference on Natural, Medical and Health Sciences and Humanities (SPIGCNMHSH 2017). An- Najah National University-Nablus. 2017.

التصميم والتشخيص الفيزيائي لأجهزة ($Ge/InSe/Ga_2S_3$) المهجنة

الملخص

في هذه الأطروحة تم دراسة وتشخيص التركيبة المهجنة على هيئة $n^+ - p$ والمصنعة من رقائق الجرمانيوم واندیوم سلناید وغالیوم سلفاید ($Ge/InSe/Ga_2S_3$) بسمك 200 نانومتر لكل واحدة منها، وقد تم استخدام طبقتي الجرمانيوم والاندیوم سلناید ($Ge/InSe$) كقاعدة لترسيب مادة الغاليوم سالفيد، وتم تحضير هذه الرقائق تحت ضغط هواء يعادل 10^{-5} ملي بار. أثبتت الدراسات البنائية والضوئية وطيف الممانعة ومنحنيات الجهد والتيار بأن التركيبة البلورية لطبقتي الجرمانيوم/ الغاليوم سلفاید (Ge/ Ga_2S_3) يسيطر عليها تركيبة الجرمانيوم، وأن تركيبة الاندیوم سلناید/الغاليوم سلفاید ($InSe/Ga_2S_3$) يسيطر عليها الشكل أحادي الميلان لمادة الغاليوم سالفيد. وقد أثبتت الدراسات الضوئية بأن تركيبة ($Ge/InSe/Ga_2S_3$) تحرف فراغات الطاقة بشكل جذري وملموس وقد تم حساب الإنفصالية في مستويات حزمة التكافؤ ومستويات حزمة التوصيل؛ يظهر من هذه القيم أن هذه التركيبة تصلح لفصل الالكترونات عن الثقوب في فضاءات مختلفة؛ مما يعيق عملية الاتحاد المباشر ويزيد من قدرة المواد على الامتصاص الضوئي. عند اجراء دراسة محوسبة لتفسير التغيرات الظاهرة في طيف العازلية تبين أن سطح هذه التركيبة مسيطر عليه من خلال التفاعلات الالكترونية- البلازمونية التي تعيق حركة الأمواج تحت التردد البلازموني في النطاق GHz 1.8-3.8، ويؤدي هذا التفاعل إلى زيادة سرعة حركة الالكترونات في المجال الكهربائي إلى 27.4 سم^2/فولت.ث. وقد أظهرت دراسة طيف الممانعة وجود مواسعة سالبة يصاحبها ظاهرة رنين عند تردد 180 MHz، وتبين من خلال حساب الانعكاس في مدى 10-1800 MHz أن التركيبة المهجنة تصلح كمرشحات لأمواج مايكرويف. علاوة على ذلك، فقد تبين من خلال دراسة منحنيات الجهد والتيار لتركيبة ($Ge/InSe/Ga_2S_3$) بين قطبين من الألمنيوم تشكيل صمامي Schottky متعاكسين ويسيطر على حركة الالكترونات الانتقال بوساطة التأين الحراري المسمى بظاهرة Schottky-Richardson. ويظهر من الدراسة بشكل عام أن التركيبة المهجنة تبدو واعدة لاستخدامها في الترانزستورات الرقيقة بحيث تعمل كأجهزة بلازمونية ومرنان مايكرويف.